

NGST integral field spectroscopy at high spectral and spatial resolution

Simon Lilly

1. Assumed NGST spectroscopic sensitivity

An $L_{AB} = 25.0$ source in 0.08 arcsec diameter pixels gives $S/N = 5$ at $R=3000$ in the continuum in 4.5 hours. This requires 17 exposures and the light is assumed to be spread over 17 pixels. $L_{AB}=25$ is $3.81 \times 10^{-33} \text{ Wm}^{-2}\text{Hz}^{-1}$ in the continuum, equivalent to $9.3 \times 10^{-20} \text{ Wm}^{-2}\mu\text{m}^{-1}$, so the equivalent line flux at $R=3000$ is $1.08 \times 10^{-22} \text{ Wm}^{-2}$ (or $1.08 \times 10^{-19} \text{ erg s}^{-1} \text{ cm}^{-2}$).

I consider the following canonical redshifts, $z = 1$, $z = 3$ and $z = 5$ (for reference, $\text{H}\alpha$ is at 3.5 microns for $z = 4.3$). I will consider an $\Omega = 0.2$ $\Lambda = 0$ cosmology with $H_0 = 65 \text{ kms}^{-1} \text{ Mpc}^{-1}$, leading to luminosity distances of 6500, 28400 and 58700 Mpc respectively. 1 Mpc is $3.08 \times 10^{22} \text{ m}$, so the line luminosities for $S/N = 5$ in 4.5 hours at $R=3000$ are $5.5 \times 10^{31} \text{ W}$, $1.04 \times 10^{33} \text{ W}$ and $4.4 \times 10^{33} \text{ W}$ respectively.

2. Line and continuum emission from star-forming galaxies

The standard “Kennicutt” relations between $\text{H}\alpha$ luminosity and star-formation rate, and the equivalent for ultraviolet “flat-spectrum” flux density, are:

$$\begin{aligned} \text{SFR (M}_\odot \text{ yr}^{-1}) &= 7.9 \times 10^{-35} L(\text{H}\alpha) \text{ (W)} \\ \text{SFR (M}_\odot \text{ yr}^{-1}) &= 1.4 \times 10^{-21} L_{\text{v}}(\text{UV}) \text{ (W Hz}^{-1}) \end{aligned}$$

So the line luminosity above corresponds to 0.004, 0.08 and 0.35 $\text{M}_\odot \text{ yr}^{-1}$ at the three redshifts considered. This is impressively low. The Orion Nebula is XXX

We can now convert a line flux detection limit to an ultraviolet continuum detection limit.

$$L_{\text{v}}(\text{uv})/L(\text{H}\alpha) = 5.6 \times 10^{-14} \text{ Hz}^{-1}$$

So,

$$f_{\text{v}}(\text{uv})/f(\text{H}\alpha) = 5.6 \times 10^{-14} (1+z) \text{ Hz}^{-1}$$

A line flux of $1.08 \times 10^{-22} \text{ Wm}^{-2}$ therefore corresponds to an ultraviolet flux density of $6.09 \times 10^{-36} (1+z) \text{ Wm}^{-2}\text{Hz}^{-1}$, or $AB = 31.24, 30.48, 30.04$ at the three redshifts of interest. This assumes no reddening, which could plausibly add about a magnitude to the ultraviolet continuum.

In terms of the continuum, the $(I-L)_{AB}$ colour of an Scd galaxy at $z = 4$ is approximately $(I-L)_{AB} = 3$, so the $L_{AB} = 25.0$ translates to $I_{AB} = 28$, or 2-3 magnitudes above the

equivalent limit for the line. This makes sense, an $R=3000$ spectrum boosts the line by $EW/\lambda \times R$. This is about 15 for a 0.5% equivalent width line (i.e. $EW_0(H\alpha) \sim 30 \text{ \AA}$).

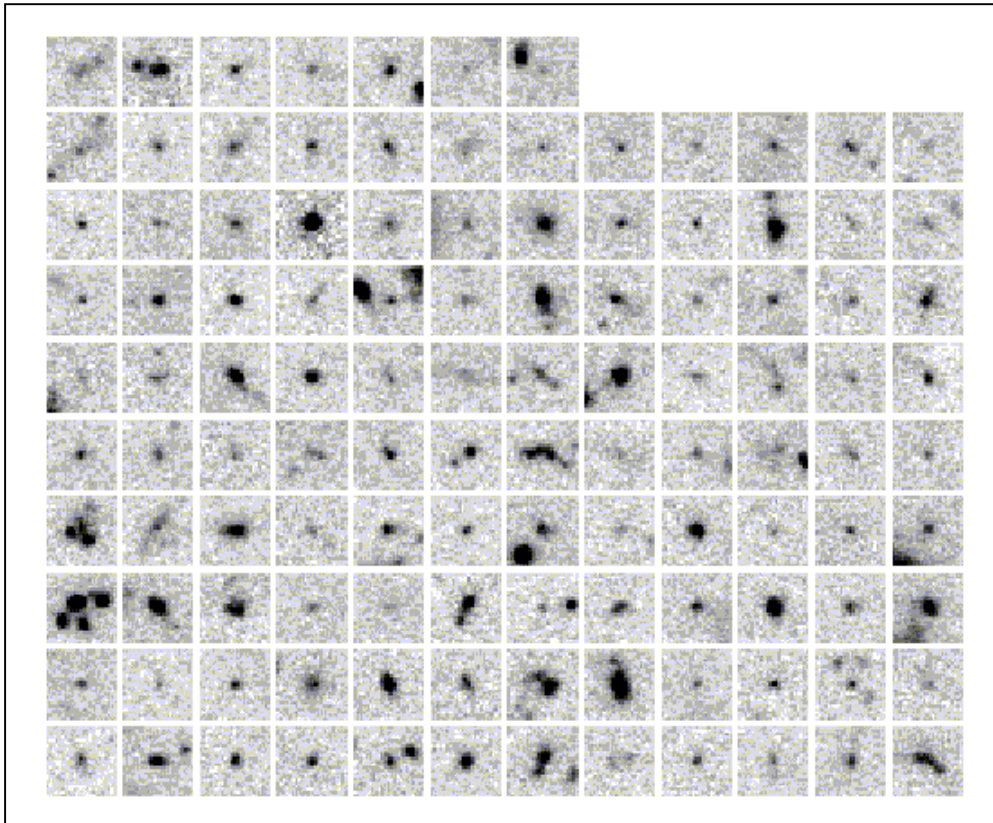
Put more directly, a surface brightness of $L_{AB} = 25.0$ per 0.08 arcsec pixel translates into $\mu_{AB}(L) = 19.5 \text{ mag arcsec}^{-2}$, equivalent to a rest-frame $\mu_{AB}(R)=14.3 \text{ mag arcsec}^{-2}$ at $z = 4$. This is remarkably high.

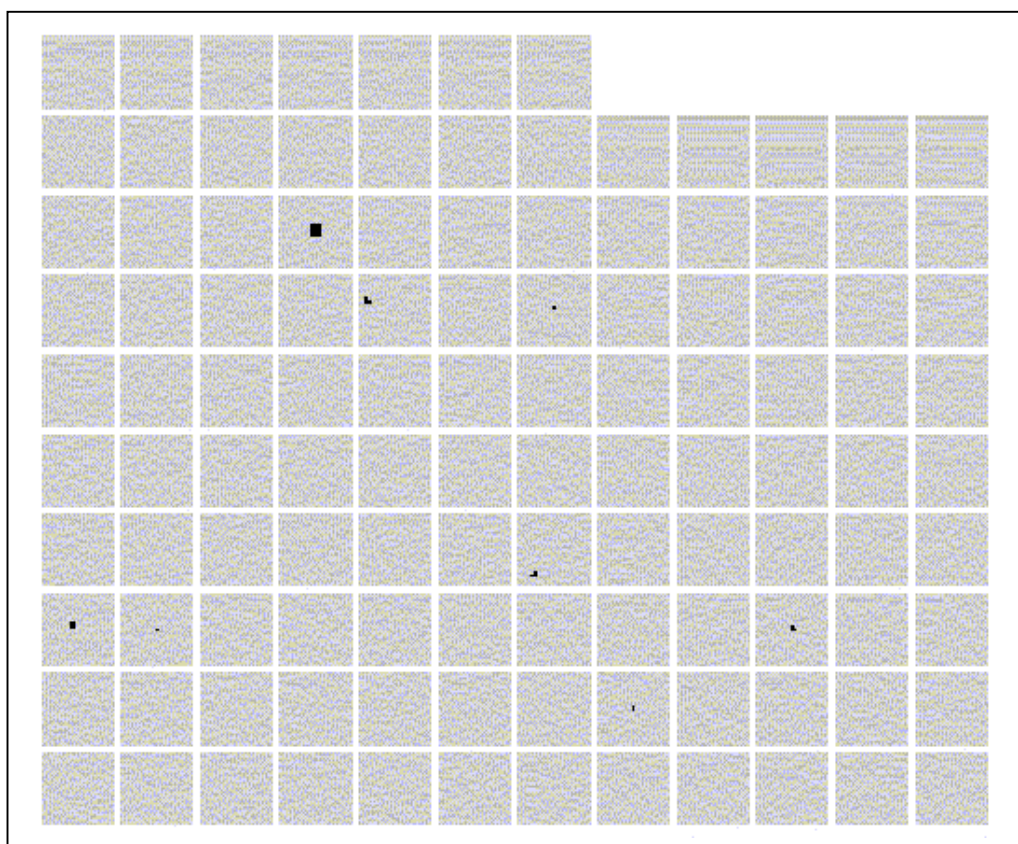
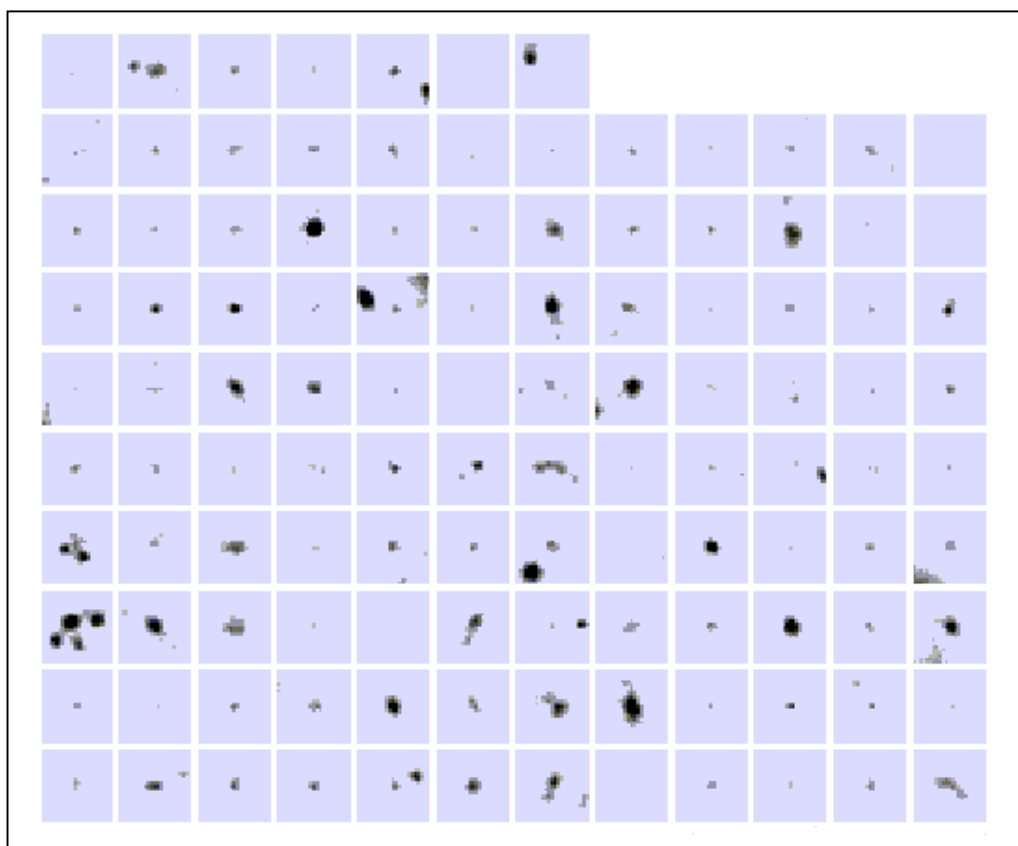
3. What fraction of galaxies at high redshift have detectable extended structure?

What fraction of the images of $3 < z < 5$ galaxies in the HDF have extended structure above these surface brightness thresholds *at the same spatial resolution*? Using the standard HDF calibration, the three effective line surface brightness limits correspond to 0.00021, 0.0004, 0.0006 counts per 0.08 arcsec pixel, while the equivalent continuum limit is 0.004 counts per 0.08 arcsec pixel.

The following three figures show the 115 galaxies in the HDF with spectroscopic or photometric redshifts in the $3 < z < 5$ range, with no surface brightness cut, and then with surface brightness cuts applied at 0.0004 counts/0.08" pixel (representing the line sensitivity) and 0.004 counts/0.08" pixel (representing the continuum).

Three mosaics of F814W images of 115 HDF galaxies with $3 < z < 6$, showing (top) all surface brightnesses, (middle) surface brightnesses equivalent to the $H\alpha$ detection threshold and (bottom) surface brightnesses equivalent to the continuum detection threshold, all at $R=3000$. Boxes are 2 arcsec to a side.





4. Summary

The conclusion is that while the continuum surface brightness limit is a real problem – almost no objects have an extended continuum surface brightness above the level of detectability in high spatial/high spectral spectroscopy, the factor of ten that you gain with plausible line emission is sufficient to bring extended structure in many objects above the threshold.

A Data Simulation Study of the NGST Multi-Object Spectrograph

Eric Steinbring

Department of Physics and Astronomy, University of Victoria,
P.O. Box 3055, Victoria, B.C., V8W 3P6, Canada
steinb@uvastro.phys.uvic.ca}

Abstract

There are many options for the design of a multi-object spectrograph (MOS) for NGST. Some proposals suggest reflective or transmissive slit-masks in the focal plane. Others promote the use of fibre bundles to feed the light to the spectrograph. Although there are many successful multiplexing instruments for ground-based astronomy, there is a lack of experience in multi-object techniques for space telescopes and so the advantages and disadvantages of the different options must be investigated. The HST gives the best idea of what to expect for deep imaging and spectroscopy with NGST, but the extrapolation is non-trivial. The NGST will be in a very different orbit, have a much larger aperture, and have more advanced detectors. This study accounts for these differences as well as simulating the operation of a multiplexing spectrograph in order to investigate the NGST MOS.

The HST NICMOS deep fields are used to generate artificial NGST NIR fields. Spectra are synthesized for objects in these fields by employing available photometric redshift data, template galaxy spectra, and model background spectra. Direct imaging with simulated filters and detectors can also be performed on these fields. In addition, a simulated NGST spectrograph can be run in a multiplexing mode and, thereby, create a virtual NGST MOS. An Integral Field Unit (IFU) is also simulated, operating as an image slicer. Results suggest that $S/N \sim 10$ spectroscopy of H(AB)-magnitude 30 galaxies will be possible with NGST. Although the NGST field is crowded at these depths, roughly 50 $1.0'' \times 0.2''$ slits per square-arcminute are possible with no spectral overlap at $R=100$. A fibre-fed spectrograph is advantageous for resolutions approaching $R=5000$ to avoid overlapping spectra.

1.0 Introduction

There are several options for the design of a MOS for NGST. They differ in their means of directing the light of the sources into the spectrograph. However, all configurations will require the determination of an optimal slit size. At the suggestion of David Crampton, a numerical simulation was designed to determine the effect of slit size on the S/N of an extracted spectrum of a galaxy.

The original test program was designed to study a single galaxy with a single slit of variable size. An archival B-band image of M51 was scaled both in pixel sampling and brightness to roughly match its appearance if imaged by NGST. Furthermore, this scaling could be altered to simulate its appearance if it were at different redshifts and for

different exposure lengths. A template spectrum of an Sb galaxy was obtained and shifted according to the user-defined redshift. By scaling the brightness of the image by the resulting SED for many wavebands, an artificial spectrum at each pixel was determined. A rectangular aperture could be selected and placed on this “spectral-image”. By applying a spectral-response curve for a broadband filter as well as the quantum efficiency for a given detector, direct imaging of this field could be simulated. The light passing through could also be dispersed to create the output of an artificial spectrograph. A region of interest could be selected from this spectrum to yield an extracted spectrum. Finally, the S/N of this extracted spectrum was output. By varying the size of the aperture the user could determine the optimal S/N. In order to determine the background light a model based on that described by Wheelock (1994) was employed. This was suggested by Simon Morris and will be discussed further below. Finally, the simulation was made even more realistic by including the effects of detector gain, readout and shot noise, and by performing the integration as a co-add of 1000 second exposures.

These investigations suggest that even an L* galaxy such as M51 would not be detected in imaging by NGST if it were at $z > 2$. This was surprising at first but others (e.g. Burgarella et al. 1998) have obtained similar results. It was also clear that S/N=10 low-resolution spectroscopy of galaxies with apparent magnitudes much fainter than $H(AB) = 30$ would require exposure times greater than 10^6 seconds.

The goal of this investigation was to determine the optimal size of slits and possibly determine advantages and disadvantages to the various mechanisms for directing the light into the spectrograph. The initial investigation was inadequate because it did not simulate a realistic galaxy field as seen with the NGST. It also had only one slit. It was clear that although the technique of simulating a spectrograph was sound, a better means of generating artificial NGST fields was needed. Furthermore, a means of expanding this single slit model to simulate a multiplexed observation would need to be devised. The method of generating artificial NGST deep fields is discussed in Section 2. The operation of the resulting simulation including a multiplexing capability is discussed in Section 3. The results are discussed in Section 4.

2.0 Generating Artificial NGST Deep Fields

To realistically simulate deep spectroscopy for NGST one first needs a realistic NGST deep field. One might begin from “first principle” and generate an entirely artificial galaxy field given an expected luminosity function, size-magnitude relation, etc. It could even include galaxy evolution. But, this approach is problematic because there will be no way to know what galaxy evolution NGST will see until NGST can observe it. An alternative is to take the deepest known NIR observations - those of the HST NICMOS deep fields and extrapolate them. This idea is similar to the method of Hubble Deep Field “cloning” by Bouwens et al. (1997). However, the goal of their method is mainly to alter the redshift distribution of the original HST WFPC2 deep fields without increasing the depth of the exposures.

The basic method adopted here is to add many new fainter galaxies to the observed deep fields - in effect, greatly increasing the depth of exposures. The simulation uses images from the HST NICMOS Deep Field South (HDFS) and photometric redshift survey data on the galaxies in this field to generate artificial NGST fields. It utilizes a model for the background illumination consisting of a scattered and thermal component of the zodiacal light. It has template spectra of four different galaxy types, E/S0, Sbc, Scd, and Irr which are redshifted according to a photometric redshift catalog. The simulated galaxies are generated by spreading the H-band HST NICMOS image over the range of 1 to 5 microns according to the expected SEDs.

Since the galaxies in the original HST field are under-sampled and noisy, in a further refinement they were replaced by artificial galaxies. These retain the spectral classification, brightness, redshift, and size of the original galaxies but these properties are used to generate highly over-sampled artificial galaxy images. These morphological templates correspond to the four galaxy spectral types and are based on a two component model of an $r^{1/4}$ -bulge and exponential-disk. The disk is augmented with spiral structures, star-formation regions, etc., based on scaling an image of the brightest low-redshift spiral galaxy available in the HDFS. The resulting template galaxies are formed with user-supplied values for bulge and disk radii, and bulge-to-total ratios. In the results discussed here, however, the original HDF galaxies were cloned into the NGST field without the complication of deriving morphological templates (the latter were necessary in a detailed study of imaging with NGST. Using galaxy image templates instead of direct clones of HDF galaxies in the spectroscopic studies did not affect the results and it is mentioned here only for completeness).

The simulation then generates the artificial NGST field by taking faint galaxies from the HDF field (say, $H(AB) > 25$), shifting them fainter by a few magnitudes and to a factor higher in redshift, making them smaller, and then putting them back into the field in randomized locations and rotations. In fact, the resulting spatial distribution of galaxies in the field is not entirely random. The galaxies are preferentially put down (according to a normal distribution with a specified 'correlation length') next to randomly chosen original galaxies. The correlation length here is the FWHM (in arcseconds) of the normal distribution. This simulates the projected spatial 'clumpiness' of a real correlation function of galaxies. The simulation actually puts several 'clones' back in the field for each faint galaxy to mimic the steep increase in source counts at these magnitudes.

The background is calculated using a model that includes both a scattered and thermal component of the zodiacal light; the scattered component is multiplied by the observed NIR solar spectrum to simulate the effects of solar absorption features.

One difficulty encountered with our simulation method occurs with overlapping galaxies. The masks used to separate galaxies are circular and the galaxies can have very small separations. In the case of extreme overlap, the average magnitude is used in the updated catalog. The spectral types may be mixed under these circumstances. That is, a portion of a galaxy might have an SED that is intermediate between the different overlapping types.

3.0 A Virtual NGST MOS

Additional refinements to the original simulated imager and spectrograph were made to enable more detailed analyses of the projects outlined in the Design Reference Mission. The filters and gratings were included with specified efficiency curves. The detector characteristics were also expanded to include size, pixel-scale, well-depth, gain, quantum-efficiency, dark current, readout and shot-noise. The user can select a particular galaxy for study from the artificial NGST deep field and perform direct imaging or spectroscopy on it. The slit size, grating resolution, and exposure duration can be input as parameters. Given values for detector size, pixel-scale, etc., the simulation outputs what the imager or spectrograph would actually record on the detector. The user can choose a region for spectral extraction and the simulation performs the reduction and extracts the spectrum. Diagnostic numbers are also output, such as the H-band magnitude and radius of the galaxy as well as S/N and resolution of the extracted spectra.

A means of simulating image-slicing was also devised. This is achieved by scanning across an approximately 2.0" x 4.0" region centered on the selected galaxy and performing slit-spectroscopy at, say, 20 positions as described above. The resulting spectra are reformatted to a single slit and recorded by the detector. Also recorded is the region covered by spectra on the detector - called the 'footprint' - which provides statistics on the efficiency of detector coverage.

Finally, a multiplexing mode was included. The number and size of spectrograph slits can be specified and they are placed on galaxies of a given magnitude selected at random. Four different focal plane mask configurations are simulated: a micro-mirror mask, a reconfigurable fibre-fed system, a slit-mask composed of sliding bands, and a micro-machined shutter mask. The latter three are comparable to those described in the Canadian NGST MOS studies. The simulation operates by 'blocking out' regions of the focal plane of the different mask configurations as each available position is used. As in the image-slicing mode, the resulting spectra on the detector and their footprints are recorded.

This method of performing virtual imaging, image-slicing, and multiplexed spectroscopic surveys with NGST was written as an IDL tool. It is included in a larger simulation of NGST instrumentation (along with a virtual Visible Imager (VI)) called 'NGST VI/MOS' (Steinbring 1999b). The goal of the investigation discussed here was to determine the optimal size of slits and compare the various slit-mask designs. The imaging mode for the MOS was included to provide a direct comparison with the VI. This was investigated by the author for the Canadian NGST VI study and will not be discussed further here. The results are available in Steinbring (1999a). The image-slicing IFU was another proposed mode for the Canadian MOS and, thus, was included for completeness.

A copy of the NGST VI/MOS software is available from the author. See also <http://astrowww.phys.uvic.ca/~steinb/> for a web-based tour of NGST VI/MOS.

4.0 Discussion/Results

The main goal of this work was to determine the S/N of extracted spectra as a function of galaxy brightness and spectrograph slit size. This is a straightforward experiment for NGST VI/MOS and was investigated using 'virtual observing runs'. Basically, the programs suggested by Lilly et al. (1998) in their Design Reference Mission (DRM) proposal were carried out with the simulation. These call for deep (10^6 second) exposures of galaxy fields. They propose low resolution ($R=100$) spectroscopy of H(AB)-magnitude 30-31 galaxies to extend spectroscopic redshift surveys to the faintest limits possible. They also propose higher resolution ($R=5000$) spectroscopy of brighter (H(AB)-magnitude 26-28) galaxies to determine characteristics of galaxy formation and evolution.

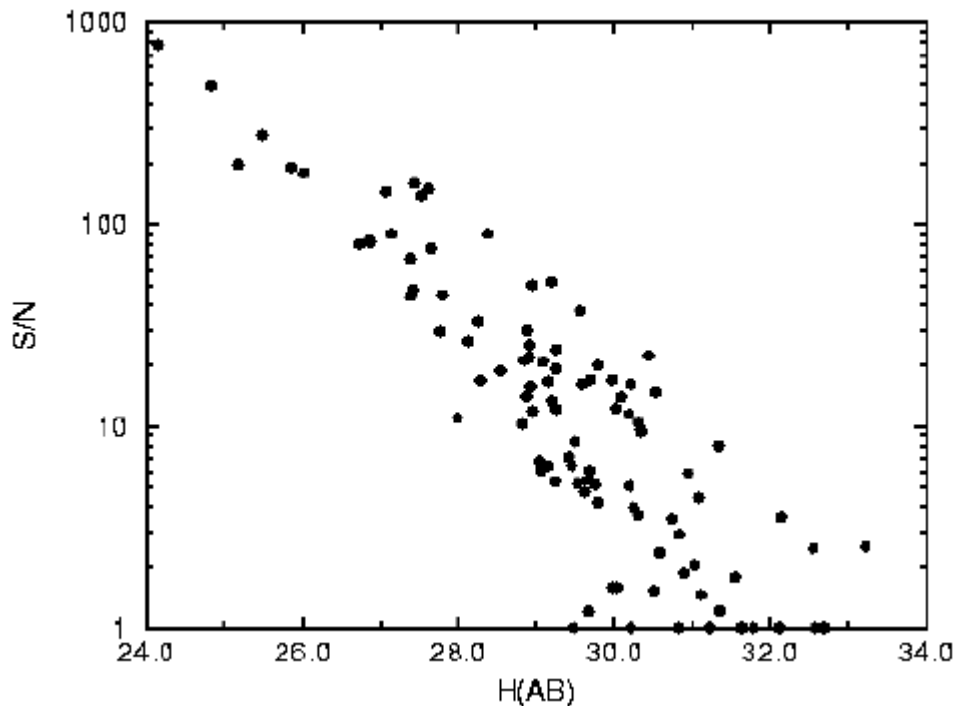


Figure 1: A plot of S/N versus H(AB) magnitudes for galaxies in the HST Deep Field South as observed with NGST MOS. Slits were $0\sqrt{\text{frcs2}}$ wide and the delivered resolution was $R=100$. The results are essentially identical for slits 0.5 arcseconds wide.

A realistic artificial field was generated. It was purposefully made to be 'clumpy'. That is, the correlation-length parameter was set to $3.0''$. This value was chosen because it is the smallest value for which severe overlapping of galaxies is not a problem. Setting this value to, say $0.5''$, will cause almost all cloned galaxies to overlap another galaxy. Setting the value to $25''$ is essentially a random distribution of galaxies on the sky. The simulation was run in multiplex mode with various slit widths and lengths. The spectrograph had 50 slits for the 50×50 square-arcsecond field. This was based on the assumption of approximately 200 slits for a 2×2 square-arcminute field for NGST. The

simulation placed slits on the first 50 H(AB)-magnitude 30-31 galaxies selected at random, performed spectroscopy and returned the S/N.

It quickly became clear that slit width is not a critical factor. Faint galaxies (H(AB)-magnitude 30-31) are small - with half-light radii of only about 0.1". The small galaxy sizes determine the resolution of the spectra. As long as the slit is not much wider than about 1.0" the increase in background light does not adversely affect the S/N of R=100 spectra. This is assuming that no other galaxy finds itself into the slit of the galaxy of interest. It is found, however, that this is often the case if the slit is wider than 0.5". Thus, the size of the slit is effectively limited by the galaxy density of the fields. These simulations also suggest that background subtraction is very effective in space. For co-adds of 1000 second exposures a calibration slit placed on the 'sky' will provide excellent subtraction of the background. This is why the slit width (in the absence of crowding by other galaxies) can be as large as 1.0". These results suggest that S/N ~10 spectroscopy of H(AB)-magnitude 30 galaxies will be possible with NGST. Although the NGST field is crowded at these depths, roughly 50 1.0" x 0.2" slits per square-arcminute are possible with no spectral overlap.

The second DRM proposal that was investigated was that of surveying relatively bright (H(AB)-magnitude 26-28) galaxies at higher resolution (R~5000). It was clear that there would be no problem concerning S/N for these galaxies. Typical S/N are in the hundreds, if not a decade more than that, for exposures of 10⁶ seconds. These brighter galaxies generally have fairly large apparent sizes, typically being larger than 1.0" across. A 0.2" slit will not have a problem with contamination by other galaxies while still providing ample light for the spectrograph. One concern, however, is that high resolution spectroscopy requires a lot of 'real estate' on the detector. Each spectrum would be at least 1.0" wide, and dispersed along 10000 pixels on the detector. Thus even if the blue end of the spectra began at the leading edge of the detector 50 galaxies would completely cover the detector with spectra. In this case, a fibre-fed spectrograph would be very advantageous for resolutions approaching R=5000. A slit-mask would always have overlapping spectra.

Most of our analyses indicate that the scientific return for microslits, mechanical slits and fibre slitlets are similar for low resolution spectra. For R=3000, the reformatting of the spectra by the fibres becomes important.

References

Bouwens, R., Broadhurst, T., Silk, J., 1997, astro-ph/9710291.

Burgarella, D., Bouwens, R., Broadhurst, T., Buat, V., Chapelon, S., Silk, J., 1998, astro-ph/9807169v2.

Burgarella, D., Buat, V., Dohlen, K., Zamkotsian, F., Mottier, P., 1998, astro-ph/9807168.

Gwyn, S., 1999, private communication.

Lilly, S., Fall, M., Stiavelli, M., Madau, P., Loeb, A., Gardner, J., Rieke, M., 1998, in The formation and evolution of galaxies I: The deep imaging survey(s), Ad-Hoc Science Working Group Design Reference Mission Proposal.

Lilly, S., Fall, M., Rieke, M., Stiavelli, M., Madau, P., Loeb, A., Gardner, J., 1998, in The formation and evolution of galaxies II: The deep spectroscopic survey(s), Ad-Hoc Science Working Group Design Reference Mission Proposal.

Steinbring, E., 1999a, A Data Simulation Study of the Next-Generation Space Telescope Visible Imager, Canadian NGST VI study, CSA.

Steinbring, E., 1999b, NGST VI/MOS: A Virtual Next-Generation Space Telescope Visible Imager and Multi-Object Spectrograph, NGST Science and Technology Exposition, Hyannis, MA, ASP Conf. Series, in press.

Wheelock, S., 1994, STScI internal report.

HST NICMOS website:

http://www.stsci.edu/ftp/instrument_news/NICMOS/nicmos_doc.html

HST STIS website: <http://hires.gsfc.nasa.gov/>

Kitt Peak Solar Observatory Data Archive website:

<http://www.nso.noao.edu/nsokp/dataarch.html>

NGST website: <http://ngst.gsfc.nasa.gov/>

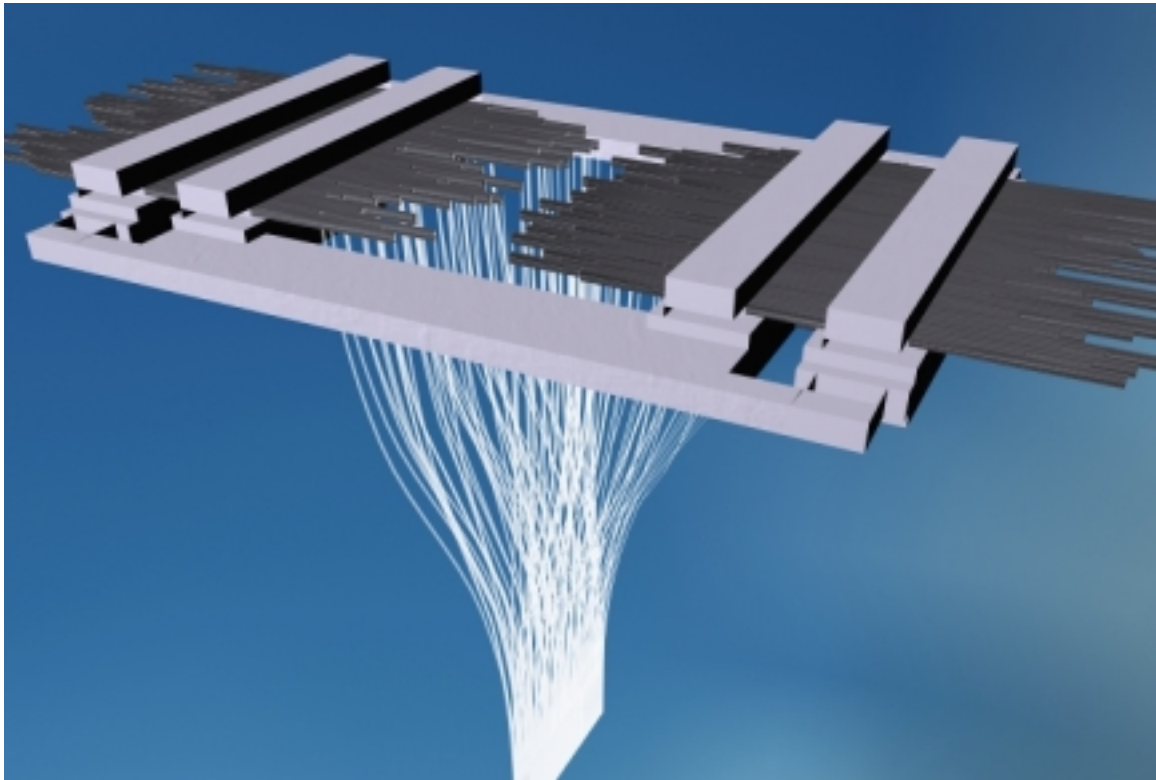
NGST VI/MOS website: <http://astrowww.phys.uvic.ca/~steinb/>

Fibre Optic Positioning Device for the NGST Multi-Object Spectrograph

D. Erickson, B. Buckham, M. Nahon & I. Sharf

bbuckham@uvic.ca derickso@uvic.ca mnahon@uvic.ca isharf@uvic.ca

Space and Subsea Robotics Laboratory
Dept. of Mechanical Engineering
University of Victoria, Victoria, B.C.
Canada, V8W 3P6



Abstract

In the scope of a prior contract, researchers at the University of Victoria's Space and Subsea Laboratory reviewed a broad range of alternatives for producing a slit mask for the space-based NGST which could be changed *in situ* for each observation. The results of that work indicated three approaches which appeared viable. Subsequent discussions with NRC staff led us to focus further efforts on the fibre-based approach which had been roughly outlined in our prior report. The purpose of the present work was to flesh out the design and bring it to the next level of definition. This report then summarizes that work, aimed at the preliminary design of a fibre-based reconfigurable slit mask for the NGST NIR Multi-Object Spectrograph (MOS).

The design requirements specified by NRC staff are first outlined, and the conceptual design of the reconfigurable slit mask is then presented. In this design, movable fibre bundles collect the incoming NIR light and reformat it for the CCD array. This design is a compromise solution in which the key priorities are: flexibility in 'slit' positioning; simplicity of mechanical design; and fault tolerance.

Two key issues are identified for further study in this work: the adequacy of fibres for transmission of NIR light at cryogenic temperatures; and the design of a mechanism to position the fibre 'slits'.

Time and resources did not allow us to study the issue of fibre adequacy in detail, and so our work in that area consisted of a review of the existing literature, as well as contacting other researchers who had prior experience in this area. Our investigation indicates that there have been substantial advances in NIR fibres for cryogenic operation during the past decade. Although there is still little information available in the public domain, all indications are that such fibres will be available in the time frame of NGST. Our main conclusions in this area, if this design is to be pursued, are that (a) better ties should be established with other groups working in this area, and (b) in-house tests of fibre properties (optical and mechanical) at cryogenic temperatures should be undertaken.

The bulk of our time and resources was channelled toward the design of a positioning mechanism for the fibre 'slits'. Our conceptual design for this device consists of (approx.) 150 bars which can be moved to programmable positions in the focal plane. In the interest of reliability and accuracy of motion, piezo-electric actuators are used for all actuation and flexures are used for all joints. The coordinated ('inchworm') actuation of a group of actuators is used to move each bar. Each bar is independent from all other bars and failure of one bar or group of actuators will not interfere with the others. Furthermore, the design allows the incorporation of redundant actuators for fail-safe operation.

A proof-of-concept device was constructed to demonstrate the viability of this approach, at least at room temperature. The device incorporates two movable bars and is controlled by a laptop PC via a custom-built set of amplifiers. The driving software accommodates different frequencies of operation and allows individual actuators to be turned off to simulate failures. It is recommended that further work on the fibre positioning device focus on the issue of operation at cryogenic temperatures.

Table of Contents

ABSTRACT.....	I
TABLE OF CONTENTS	II
1. INTRODUCTION.....	1
2. CONCEPTUAL DESIGN	2
2.1. NEAR-INFRARED FIBRE OPTICS	6
2.1.1. <i>Past and Present Cryogenic Developments</i>	6
2.1.2. <i>Commercial Supply of NIR Transmitting Fibres</i>	7
2.1.3. <i>Design Issues / Optical Performance</i>	15
2.1.4. <i>Summary</i>	17
2.2. PIEZO ELECTRIC ACTUATORS	19
2.2.1. <i>Specifications and Power Consumption</i>	20
2.3. SAFETY AND REDUNDANCY	21
2.3.1. <i>Independent Movable Bars</i>	21
2.3.2. <i>Redundant Actuators</i>	21
2.3.3. <i>Other Technologies</i>	21
2.4. ADDITIONAL OPTIONS	22
2.4.1. <i>Image Slicer</i>	22
2.4.2. <i>Optical Position Feedback</i>	23
2.4.3. <i>Multiple Fibre Sizes</i>	23
2.4.4. <i>Long-Stroke Operation</i>	23
3. PROOF OF CONCEPT DEVICE.....	24
3.1. COMPONENT PHOTOGRAPHS.....	25
3. 2. PIEZOELECTRIC CONTROLLERS.....	27
3.2.1. <i>Control of Clutching Actuators</i>	27
3.2.2. <i>Control of Carriage Actuators</i>	28
3.2.3. <i>Frequency Issues</i>	28
3.3. PERFORMANCE	28
4. CONCLUSIONS	30
5. RECOMMENDATIONS.....	30
6. REFERENCES.....	32
APPENDIX A: PIEZO CALIBRATION CURVES	33
APPENDIX B: COMPUTER CONTROL SYSTEM	40
RUNNING THE PROGRAM.....	40
SOFTWARE TROUBLESHOOTING.....	41
CUSTOMIZING THE MOTION	41

1. Introduction

A preliminary investigation into creating a slit mask for the NGST MOS was completed by the Space and Subsea Robotics Laboratory at the University of Victoria in January, 1999 [1]. A diversity of methods was considered and three of these were identified as the most promising: laser machining, ionized particle deposition, and reconfigurable arrays of fibre optic bundles. Following the review of those results by DAO, the UVic group was tasked with performing a more detailed investigation of one of the more promising alternatives, the fibre optic bundle solution, culminating in a proof of concept device. This report summarizes the results of this work.

Several factors form the basis for selecting the fibre optic solution to create slit masks for NGST MOS:

- In-situ manufacturing methods such as laser machining and ionized particle deposition inherently involve the production of waste material, which could contaminate the optics of the NGST.
- A reconfigurable array of fibre optic bundles does not require the storage and manipulation of raw materials.
- Fibre optic technology has been accepted in the astronomical community, and a basis of expertise has been developed over the last 15-20 years.

To briefly summarize the fibre optic solution, the slit mask is made up of fibre optic bundles which are to be placed in the focal plane at the desired slit locations. The design of such a device involves two critical aspects: optical fibres capable of transmitting near-infrared (NIR) wavelengths at cryogenic temperatures and a mechanical positioning device for placing fibres in the focal plane. The latter must be subject to the constraints and criteria specified below.

Constraints:

Mask area	180 x 180 mm
Number of slitlets	> 100
Nominal slitlet size	2 mm x 200 μ m
Positioning accuracy	< 10 μ m
Relative positioning accuracy	20 - 50 μ m
Reconfiguration time	< 20 min
Operating environment	30K, vacuum

Criteria:

- Minimize heat generation
- Minimize power consumption
- Maximize the focal plane fill factor
- Maximize the number of slitlets

With regard to the optical fibres, several research groups and companies are currently working on developing fibres for NIR wavelengths. These fibres are being examined for their optical (throughput, FRD) and mechanical (strength, bend radii) properties. At this time, the Space and Subsea Robotics Laboratory at the University of Victoria is not equipped to test NIR fibres at cryogenic temperatures. As part of this work, a survey was conducted for availability of fibres suitable for the present application. It was found that this technology is developing rapidly and it is likely that fibres will be available to meet the NGST operating conditions. The results of our survey of NIR fibres are given in Section 2.1, and the remainder of this report focuses on the development of a manipulator which is capable of positioning many fibre optic bundles in the telescope focal plane.

2. Conceptual Design

The goal of this design work is to develop a concept for a device that is capable of positioning fibre optic bundles or slitlets within the telescope focal plane. Figure 2.1 presents the components of the conceptual design:

- *Frame*: surrounds the focal plane and provides a platform to support the rest of the components.
- *Blade flexures*: connect the carriage to the frame. The blade flexures allow a small range of carriage motion in one direction.
- *Carriage*: generates the stepwise motion of the movable rods
- *Upper and lower carriage covers*: seal the cavity inside the carriage. The lower cover acts as a mounting plate for the clutch piezos. The upper cover acts as a sliding surface for the movable bars.
- *Movable bars*: support the fibre slitlets.
- *Guide posts*: constrain the motion of the movable bars.
- *Clamping bar*: used as a foundation for the clutching of the movable bars.
- *Clutch piezos*: are contained in cavities in the frame and the carriage. These piezos are used to press the movable bars against a clamping bar.
- *Actuator piezos*: are used to pull the carriage towards the frame. One side of the actuator piezo is fixed to the frame the other is coupled to the carriage.

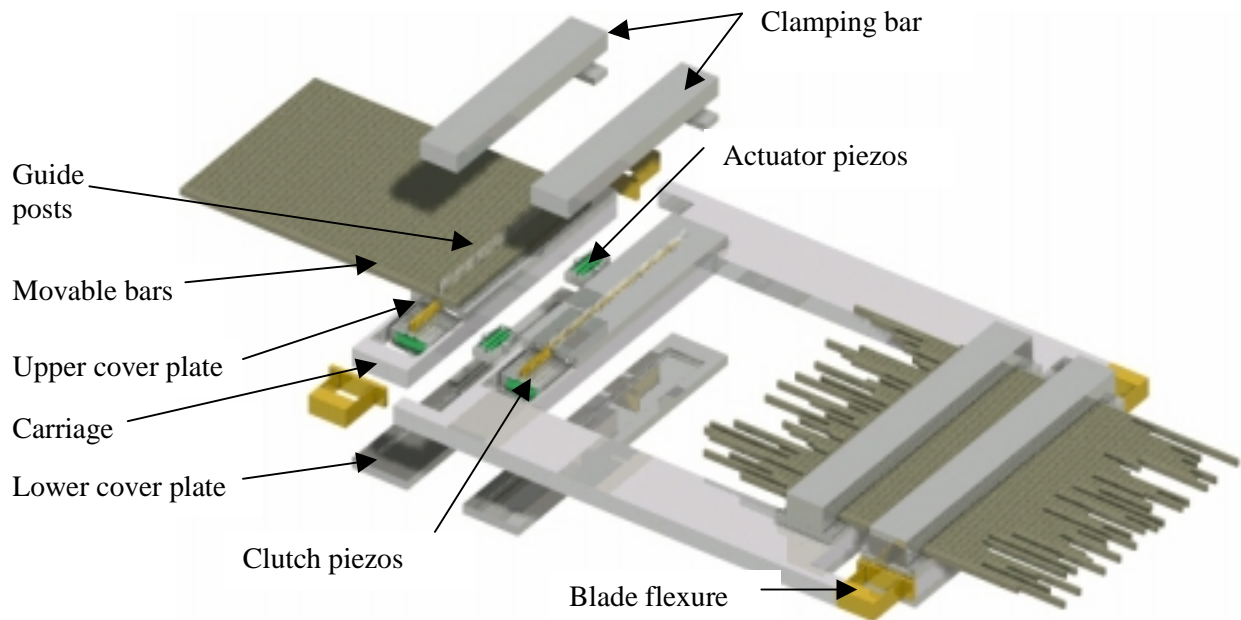


Figure 2.1. An exploded view of the conceptual fibre optic manipulator.

Each slitlet is assumed to be a linear array of fibres which collect light from a rectangular region that is $2\text{mm} \times 200\mu\text{m}$. It is assumed that the slitlets are oriented in the same direction, and are located in one or more columns or banks. This is a common arrangement used in slit masks for ground based spectrographs. For the conceptual design, we have chosen to move the slitlets across the focal plane in a linear fashion from two sides. This results in two banks of slitlets, with 60-90 slitlets per bank, as illustrated in Figure 2.2.

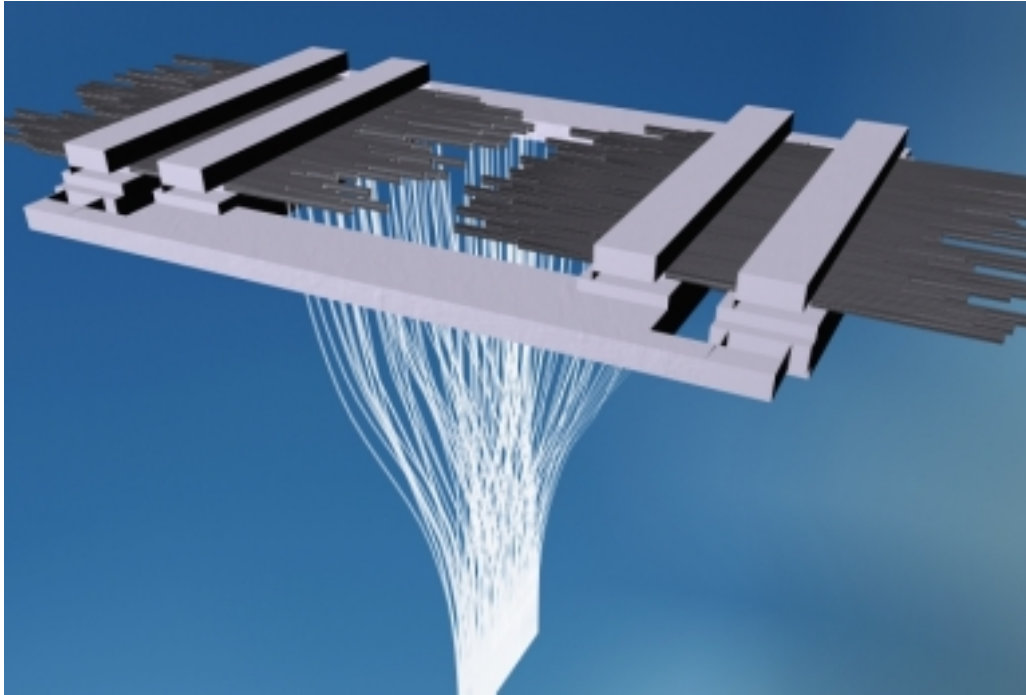


Figure 2.2. Conceptual design of NGST MOS fibre manipulator

Each individual bundle of fibres is attached to the tip of a movable bar which is actuated using "inchworm" linear motion. This type of motion has been used for actuation by companies such as Burleigh Instruments. However, it has been significantly altered in this device to actuate multiple bars in parallel. The movement of a single bar is achieved through the co-ordinated action of three piezo electric actuators. Each bar has two "clutch" piezos which are used to clamp the bar to either a fixed or movable surface. The third piezo is an "actuator" which moves the sliding bars across the focal plane. Since the stroke of piezo actuators is very limited (microns), the movable bars are translated in small steps. Long stroke linear motion is achieved by taking thousands of steps. One cycle of this motion is shown in Figure 2.3 in section view. The clutch piezos move vertically to clamp the movable bar against the upper surface while the actuator piezo moves horizontally to generate the translational motion. By co-ordinating the motion of the piezos, the movable bar is made to move one step to the right.

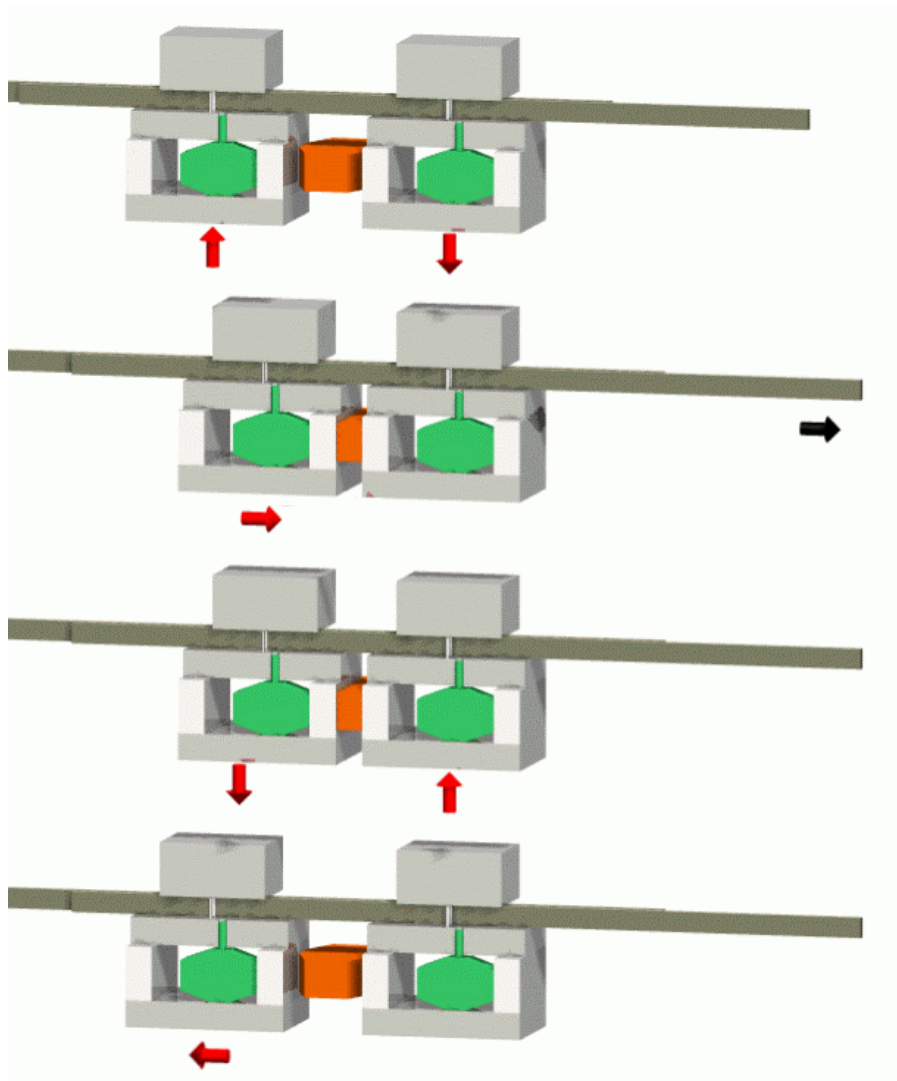


Figure 2.3. Linear motion using piezo actuators and "inchworm" motion

While the movable bars control the position of the slit inlet, the output of all the slitlets is reformatted in one long slit at the entrance to the spectrograph. This has certain astronomical advantages over conventional slit mask spectroscopy, most notable is the ability to create high resolution spectra which utilize the entire detector area.

Rows of lenslets attached at the inlet of the fibres create the "slitlets". These lenslets could be used to collect light from a rectangular region and direct it into the core of each fibre (see Figure 2.4). They could simultaneously be used to change the input $f/\#$ of the beam to reduce the FRD effect and maximize the fibre throughput. Additional rows of fibres and lenslets could be added to give 2D spatial information. Output microlenses could also be used at the entrance to the spectrograph, reformatting the beam to the desired $f/\#$ and maximizing throughput.

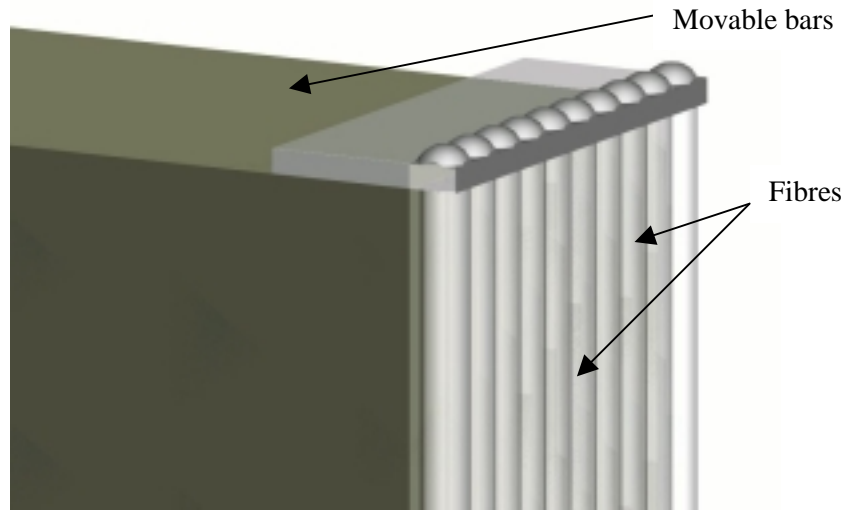


Figure 2.4. Fibre optic slitlet with attached lenslet

Central to the proposed design concept is the use of infrared fibre optics for making up the slits, and the application of piezo electric actuators to move fibre bundles to desired locations. As noted in the Introduction, a survey of available fibre optics technologies has been conducted, the results of which are presented in the following section. In Section 2.2, we discuss the piezo actuators used in the proof of concept device. Our design also incorporates a number of desirable features such as safety, redundancy and it offers the flexibility to include many additional options. Since these topics are central to the success or failure of the device, they are discussed in more detail in Section 2.3.

2.1. Near-Infrared Fibre Optics

A detailed investigation of fibre optic technology has been performed which focussed on:

- 1) Summarizing the extent of past cryogenic testing of suitable NIR transmitting fibres.
- 2) Determining the design issues for the application of glass fibres on the NGST MOS unit.
- 3) Finding optical fibres with suitable transmission characteristics in the NIR band.

2.1.1. Past and Present Cryogenic Developments

Near infrared (NIR) transmitting fibre optics is a relatively new technology. In the past most of the NIR observation performed with fibre based systems has been limited to wavelengths less than $2.2\mu\text{m}$, as this was the upper limit on the transmission of ultra low OH^- silicate fibres. For transmission in the $1\text{-}5\mu\text{m}$ band of wavelengths two materials are prevalent, zirconium fluoride glasses and chalcogenide glasses. While there is some documentation regarding the mechanical (bend radius, tensile strength, elasticity) and optical properties (throughput, FRD, NA) of IR fibres provided by manufacturers at

room temperature, there is virtually no documentation regarding the behavior of these fibres at relatively standard cryogenic temperatures (liquid N₂).

The only literature that has been found regarding cryogenic experimentation was an effort of Ken Levin at Infrared Fibre Systems (IFS) and Dave Glenar at the Goddard Space Flight Center [2][3]. They tested the transmission properties of IFS fluoride fibres at liquid N₂ temperatures, but did not publish any testing of the fibre mechanical properties. Their documented experimentation led to Ball Aerospace ordering bundles of IFS fibres for use in the NICMOS unit of the HST. Ball completed in house vibration and temperature experiments, but we have not been able to locate these results to date. Eventually the fibres were eliminated from the NICMOS design. The IFS fibres are currently being used by the Goddard Space Flight Center in the development of the CIRCLE suite of instruments for the Rosetta comet lander mission [4]. A bundle of IFS fibres is to be used as a cable for a remote sensor and deployed into holes drilled into the comet surface. Dave Glenar and researchers at the JPL are currently faced with similar problems to those posed by this project: to characterize the optical and mechanical behavior of the IFS fibres at a cryogenic operating temperature. That project is focussing on 400µm core IFS fluoride glass fibres.

Some additional astronomic projects are also driving more experimentation with NIR fibres. At the Anglo-Australian Observatory (AAO), David Lee and Roger Haynes will be commencing cryogenic testing of low OH⁻ silicate and fluoride glass fibres in June of 1999 as part of the development of the Gemini IR IFU/MOS unit. These silicate fibres are good (<1dB/m attenuation) out to wavelengths of 2.2µm - 2.5µm. David Lee at the AAO has already completed some informal tests in which silicate fibres were manipulated in liquid N₂ baths to test their flexibility. No noticeable changes in the flexibility of the silicate fibres were reported. In [5] and [6] it is presented that glasses by nature shouldn't show large changes in their mechanical properties when cooled from room to cryogenic temperatures. This gives us basis to hope that the fluoride fibres will maintain a good portion of their flexibility at the operating temperature of the NGST.

2.1.2. Commercial Supply of NIR Transmitting Fibres

Chalcogenide or fluoride glass fibres are known to be significantly more fragile than optical fibres constructed from silicate glasses. They also appear to be less readily available. Five suppliers of chalcogenide and/or fluoride glass fibres have been located:

Seiche River Photonics/Le Verre Fluore (LVF)

Redondo Beach, CA, USA

Contact: John Bessey

ph: (310) 849-0001 fax: (310) 798 0897

email: brekilien@worldnet.att.net

Institute Nationale Optique (INO)

Sainte-Foy, QC, CA

Contact: Jocelyn Lauzon or Serge Caron

ph: (418) 657-7406 fax: (418) 657-7009

email: lauzon@ino.qc.ca, scaron@ino.qc.ca
www.ino.qc.ca

Amorphous Materials Inc. (AMI)

Garland, TX, USA
Contact: Greg Whaley
ph: (972) 494-5624 fax: (972) 272-7971
email: GegWhaley@aol.com
www.amorphousmaterials.com

Infrared Fibre Systems (IFS)

Silver Spring, MD, USA
Contact: Ken Levin
ph: (301) 622-9546 fax: (301) 622-7135
email: info@infraredfibresystems.com
www.infraredfibresystems.com

Galileo Corp.

Sturbridge, MA, USA
Contact: Brian Lincoln
ph: (508) 347-4204 fax: (508) 347-3849
email: BLincoln@Galileocorp.com
www.galileocorp.com

From the constraints and criteria of the NGST MOS Phase I study, the necessary throughput of the fibres must be $\geq 90\%$. The following transmission plots, and additional product information have been provided for comparison.

LVF

Seiche River Photonics is the North American supplier of Le Verre Fluore fibre optic products. Le Verre Fluore is based in Brittany, France and is believed to be the first supplier of commercial zirconium fluoride glass fibres. They produce three different IR fibres (fibre guides): IRguide-1, IRguide-2, and IRguide-3. It should be noted that the lower limit on the range of temperatures over which the LVF fibres can be used is in the cryogenic realm. Under standard atmospheric conditions, the LVF products have compared favorably to their chief competition, the IFS fibres. However, in [7] the LVF and IFS products were both tested for FRD effect, and the LVF product was noticed to exhibit a worse FRD effect. However, it was believed that this was due to impurities in the fibre at that time which created fluctuations in refractive index.

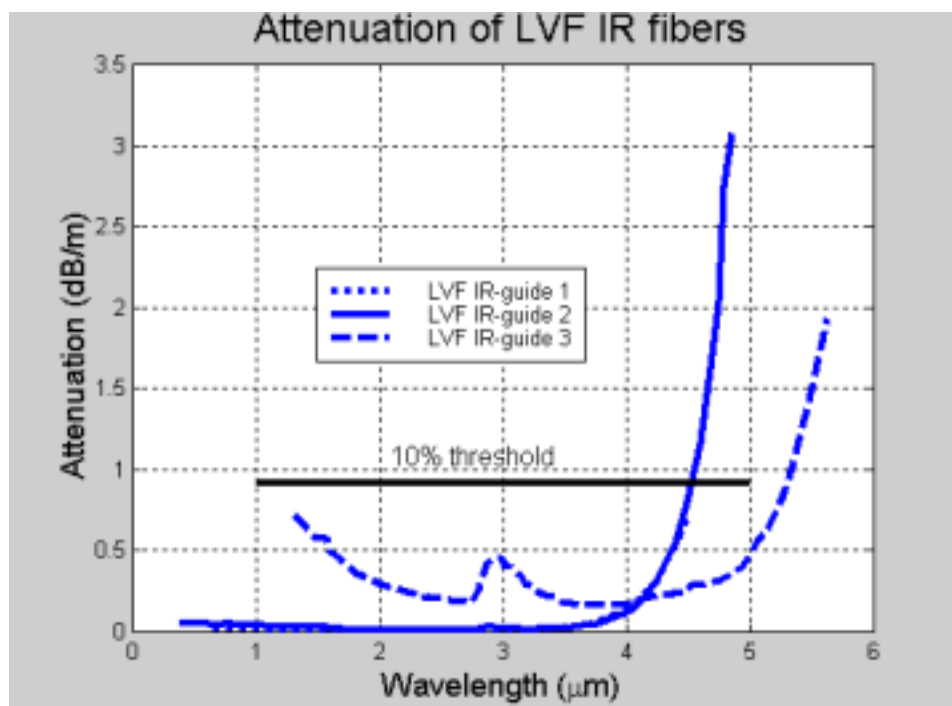


Figure 2.5. LVF IRguide fibre transmission at room temperature.

LVF - IRguide Fibre	
Numerical aperture*	0.2 - 0.45
Core diameter	70, 100, 150, 200μm
Temperature range	63K - 323K

*Numerical aperture can be specified in any order placed to LVF.

INO

INO is a private non-profit corporation established by the NRC. Much of the research performed at INO is aimed at determining fluoride glass structures that optimize the mechanical performance of the fibres. In conversation with Serge Caron, minimum bend radii of 4mm have been quoted for 60μm core / 125μm clad fibres. INO has also performed informal cryogenic tests by immersing the fluoride fibres in liquid N₂. No mechanical failure was noted in these tests. INO is currently implementing the necessary quality control technology for the commercial production of high quality ZBLAN fluoride glass fibres. The attenuation characteristics of the INO fibre are shown in Figure 2.6. INO has expressed an interest in collaborating on the NGST MOS project.

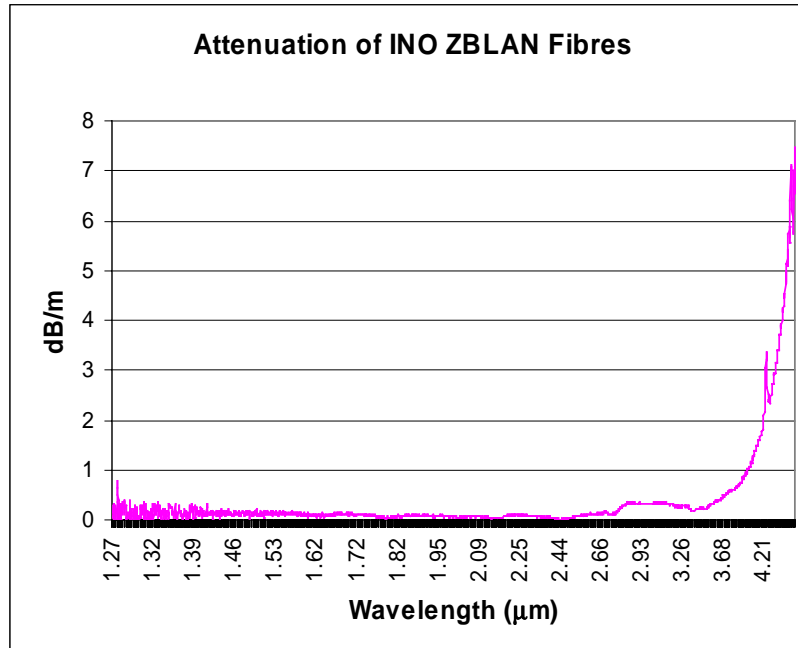


Figure 2.6. Attenuation data for the INO 60μm core / 125μm glass core glass clad fibre.

AMI

Since 1990 AMI has been manufacturing chalcogenide glass fibres. The chalcogenide glasses are compositions of arsenic, selenium, and tellurium. They feature two products, a C1 fibre for near to mid-IR transmission (2.5μm -10μm) and a C2 fibre for near-IR transmission (1μm -5.5μm). Conversation with experts in astronomical fibres revealed the opinion that chalcogenide fibres are unlikely to be able to compete with the transmission offered by fluoride glass due to the absorption spikes in their transmission plots, which are shown in Figures 2.7 and 2.8.

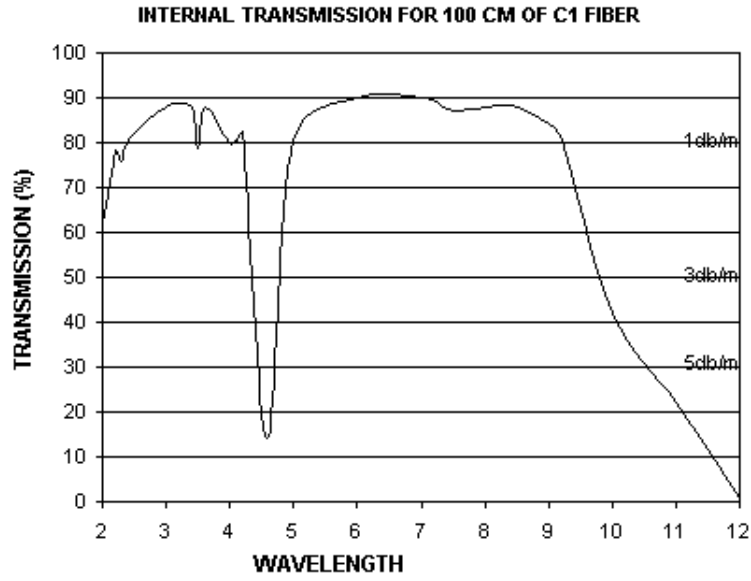


Figure 2.7. AMI - C1 fibre transmission

AMI - C1 Fibre	
Numerical aperture	0.5 - 0.7
Core diameter	< 100, 100, 250 μm
Index of Refraction (n)	2.81 - 2.82
$\Delta n/\Delta T$	$3 \times 10^{-5}/\text{K}$
Bend Diameter (@ core diameter)	0.2 cm (100 μm) 1.6 cm (500 μm)
C.T.E.	23.5/K
Temperature range	< 443K

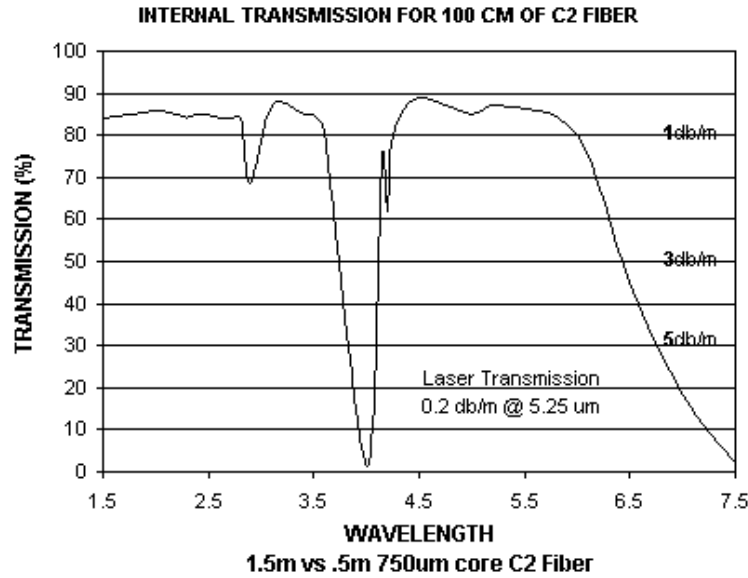


Figure 2.8. AMI - C2 fibre transmission

AMI - C2 Fibre	
Numerical aperture	0.5 - 0.7
Core diameter	< 100, 100, 250 μm
Index of Refraction (n)	2.38 - 2.41
$\Delta n/\Delta T$	$0.9 \times 10^{-5}/\text{K}$
Bend Diameter (@ core diameter)	0.2 cm (<100 μm) 1.6 cm (500 μm)
C.T.E.	21.4/K
Temperature range	< 481K

IFS

IFS is the best known North American supplier of NIR transmitting fibre products. The IFS products have been well documented in literature [7], and results of cryogenic transmission testing of these fibres have been published [2] [3]. In [7] it was revealed that the IFS fibres exhibited less FRD effect than the LVF products. Figure 2.9 gives the attenuation plot for the SG (sensor grade) type fibre produced by IFS for both plastic and glass clad fibres. For reasons that are outlined in Section 2.3, and the better performance of the glass clad product, we are focussing on the glass clad fibre.

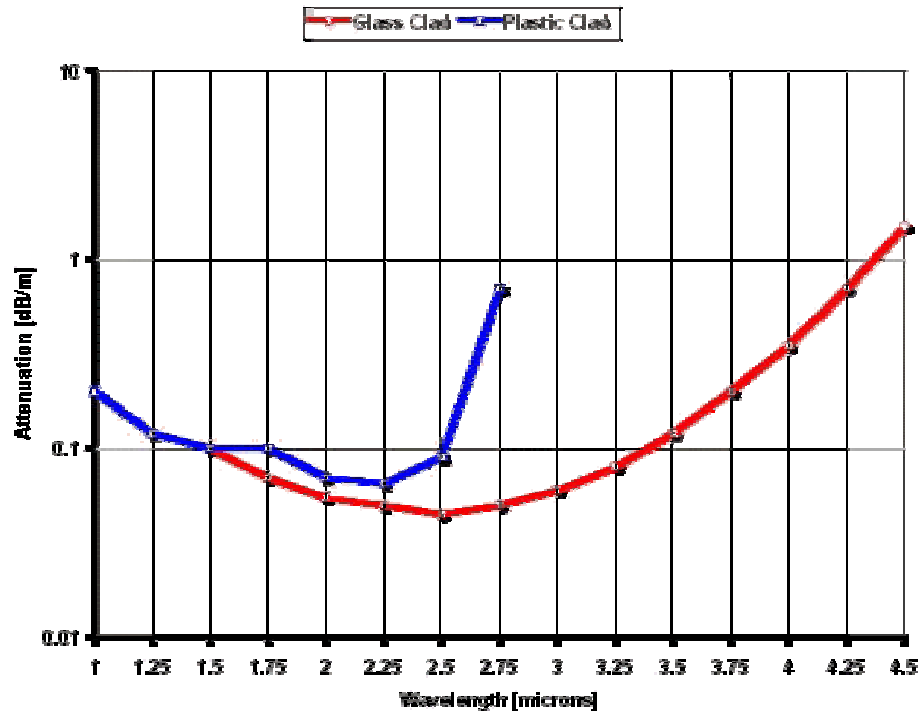


Figure 2.9. IFS - SG fibre attenuation

IFS - SG Fibre	
Numerical aperture	0.22 (glass clad) 0.6 (plastic clad)
Core diameter	100, 200 μm
Bend Diameter (@ core diameter)	1.2 cm (200 μm)
Temperature range	< 523K

Galileo

The Galileo Corp. produces both chalcogenide glass and heavy metal zirconium fluoride glass (HMFG) fibres. While the transmission bandwidth of the chalcogenide fibres is wider (1 μm - 10 μm), the transmission borders on the 90% constraint. Also, it is noted that for both suppliers of chalcogenide glasses (AMI and Galileo), a sharp attenuation spike is evident at 4.2 μm - 4.5 μm depending on the specific chalcogenide fibre. As this spike is a characteristic for chalcogenide fibres from two independent manufacturers, it is believed to be a reflection of phonon absorption that is inherent with the chalcogenide structure. Figure 2.10 also illustrates how the transmission of the low OH⁻ silicate glasses degrades drastically at 2.2 μm .

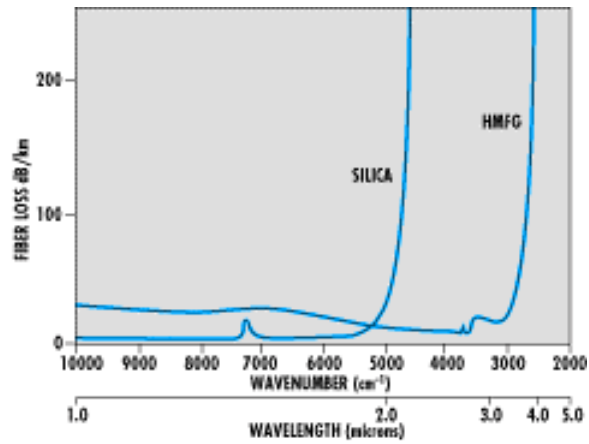


Figure 2.10. Galileo Silica and HMFG fibre attenuation

Galileo - HMFG Fibre	
Numerical aperture	0.37
Core diameter	250 μm
Bend Diameter (@ core diameter)	10 cm (250 μm)
Temperature range	253K - 358K

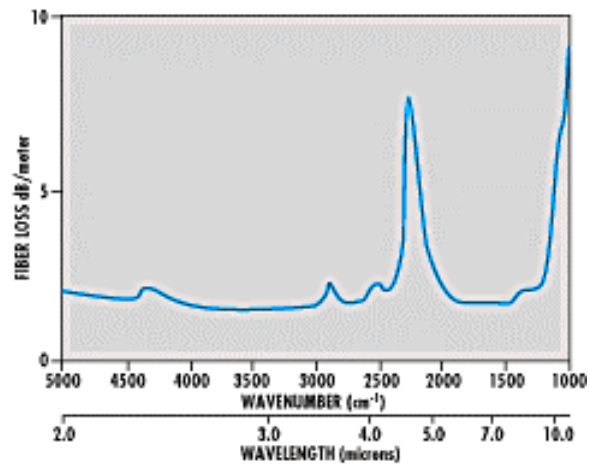


Figure 2.11. Galileo Chalcogenide fibre attenuation

Galileo - Chalcogenide Fibre	
Numerical aperture	>0.3
Core diameter	750 μm

Bend Diameter (@ core diameter)	20 cm (750 μ m)
Temperature range	253K - 358K

2.1.3. Design Issues / Optical Performance

In conversation with Dave Glenar at the Goddard Space Flight Center, it was highlighted that any mechanical failure of fibres at cryogenic temperatures would likely be preceded by degradation in the fibre's optical properties caused by any internal mechanical stresses. Thus, it is his belief that maintaining the optical performance of the fibre at the cryogenic operating temperature becomes the limiting requirement. A description of the criteria which will determine the optical performance of any NIR fibre, and the manner in which temperature dependent mechanical properties affects each, is given below.

Transmission

In [3] it was noted that the transmission of IFS fluoride fibres improved when the fibre was cooled to liquid N₂ temperatures. This was attributed to a decrease in the phonon absorption of the material, the prime mode of attenuation at longer wavelengths. This suggests that the transmission/attenuation curves given above could show an extension in the range of adequate transmission. Generally adequate transmission is defined by attenuation <1dB/m (90%).

Focal Ratio Degradation (FRD)

Focal Ratio Degradation (FRD) is the transfer of light energy in a fibre from one mode to another that is a result of inconsistencies in core diameter and refractive index along the length of the fibre. Such variations cause propagating rays to reflect off the core-cladding interface with varying angles of incidence, and cause higher order modes of propagating light (light that is incident on the core-cladding interface with a large angle of incidence) to be lost to the cladding [8]. Fibre systems with fast input focal ratios (numerically small f/#) exhibit less FRD. The FRD effect always acts to decrease the output f/# (or speed up the output).

During the transition to cryogenic temperatures, the cladding may contract about the core of the fibre if there is a significant difference in the thermal expansion coefficients between the core and cladding material. If such a stressing of the core material occurs, small microbends can develop which increase the FRD effect. Thus even if the FRD is characterized for a fibre and aft optics are designed to contain the speed of the fibre output, the drop to cryogenic temperature can cause the FRD effect to worsen, the aft optics to be overfilled, and the throughput to drop significantly. For this reason it is desirable to keep the materials used for cladding and core as homogeneous as possible. Thus, only glass core-glass clad fibres have been considered.

It is well recognized that the mounting of the fibres has a great effect on the level of FRD that is experienced. With identical lengths of fibres, different levels of FRD have been recorded [8]. Such differences can be induced by inconsistencies in how the fibre ends are fixed to a manipulator tip. The number of variables present in any FRD characterization make published or documented FRD results questionable. For

example, experiments at the AAO have shown a 10% decrease in throughput at cold temperatures that is attributed to FRD, while work at Durham University has shown no appreciable increase in the FRD effect with change in temperature.

Numerical Aperture (NA)

In order to limit the contraction of the cladding onto the core, as mentioned above, the fibres being considered are a glass core/glass clad fibre. Unfortunately, this also results in a relatively small difference between the index of refraction between core and cladding material, and thus smaller numerical apertures and acceptance cones for the fibre candidates. This acts as a limit on the speed of the image at the input to the fibre. Since the FRD effect can be reduced/eliminated by speeding up the input at the fibre inlet [8], a small numerical aperture will act to create a more significant FRD effect. Thus the greater the difference between the index of refraction of the core and the cladding, the better. Another way to combat the negative effects of a small numerical aperture is to increase the core diameter. In this approach we are constrained by the slit width constraint of 200 μ m. Should this constraint be flexible, it could be advantageous to increase the slitlet width. Another option is to use lenslets. Lenslets would have to be mounted onto the fibre ends or drawn from the fibre core material itself in a manner described in [9]. This latter approach would remove the problems associated with bonding the lenslets to the fibre in a cryogenic environment.

Thermal Dependence of the Index of Refraction (n)

The propagation of light down a fibre depends on the phenomenon of total internal reflection. Thus the index of refraction of the core is greater than that of the cladding. However, the index of refraction of a material is dependent on temperature. As the temperature drops the index of refraction of the cladding can increase, and the attenuation jumps significantly. It is possible that the wave guiding capability of the fibre will be lost completely, and that any transmission will become due to reflection off of a buffer coating. This phenomenon is material dependent. Given the IFS testing at liquid nitrogen temperatures showed an improvement in transmission, one could hypothesize that the fluoride fibres should not lose their waveguiding capabilities at the NGST operating temperature.

Flexibility

It has been shown that, at room temperatures, macrobends (large scale bends or curves in the fibre) do not contribute to the FRD effect. However, if cooling to the operating temperature should significantly increase the Young's modulus of the core or cladding of the fibre, any macrobending of the fibre induced by manipulation of the fibre inlet will generate additional stress which can create microbends [8]. It is believed that the most significant restriction on the flexibility of the cable will be the flexibility of the buffer coating at the operating temperature [10]. This opinion is reinforced by the good mechanical performance of silicate glass fibres after being dipped in liquid N₂ in the AAO tests. Due to the relatively small motions required of the inlets of the fibre slitlets, it is not expected that the manipulation of the fibre will create significant problems.

Mounting fibre Inlets

In order to avoid stress induced by microbends, low shrinkage, slow curing epoxies are recommended when attaching the fibres to a manipulator tip or stationing fibres in a

hardwired configuration. Even when using such adhesives, it has been found that the curing of the epoxy can increase the FRD and cause the throughput of the fibre to overfill the aft-optics designed for the normal FRD of the fibre [8]. A popular method of mounting fibres is to use precision grooves in a thermally matched metal ferrule, and tack the fibre in place with one or two beads of low shrinkage epoxy, well away from the fibre end. Ian Parry of the Institute of Astronomy at Cambridge University has used this simple approach in the COHSI unit, and he claims it performed adequately [11].

There is also insufficient publicly available data to address another issue: how a curved section of fibre will behave when cooled. We have questions as to how the thermal contraction of the fibre will affect the curvature of any section of fibre. By understanding the changes in curvature that a curved section of fibre will undergo when cooled to 30K, an optimal mounting scheme can be determined to link the focal plane to the spectrograph. The mounting of the fibres may also affect the manipulator design in terms of the fibre terminations at the tip of the manipulator(s).

2.1.4. Summary

Although there is very little published, quantitative data regarding the optical and mechanical performance of NIR transmitting glass fibres, the possibility of using fibres in the NGST MOS seems favorable for a couple of reasons. Firstly, fibre technology in the 1-5 μ m range is rapidly evolving. This is evidenced by the development of the IRguide-3 fibre at LVF, which has a suggested permanent operating temperature of ≥ 63 K. Secondly, the development of the CIRCLE suite of instruments and the NIR fibre probe for the Rosetta comet lander mission demonstrates that the aerospace community believes that glass fibres can be employed in space applications. This is also supported by the cryogenic testing of fibres at the GSFC in the late 80's. In fact, glass fibres have already been considered for use in space with the NICMOS unit of the HST.

The choice of fibres for this project seems to be limited to various fluoride glass products. These fibres demonstrate transmission that is a few percentage points better than the alternative product, chalcogenide glasses. Chalcogenide glasses also exhibit characteristic attenuation spikes at 4.2 μ m - 4.5 μ m, depending on the particular molecular makeup of the chalcogenide glass. Although fluoride glasses have a shorter range of transmission, they do perform adequately (<1 dB/m) out to 5 μ m. One can also expect the range of transmission to increase by at least 0.3 μ m due to the decreased phonon absorption capability of any glass fibre at cryogenic temperatures. The choice of fibres must also be constrained to those of a glass core, glass cladding construction. By maintaining a more homogeneous composition, the effects of thermal expansion (increase in the FRD) can be minimized.

It is evident that the optical requirements of a fibre used in the NGST MOS will provide the strictest performance criteria. By achieving the transmission requirements and exhibiting the minimal FRD inherent in any fluoride glass fibre, a fibre must avoid initial stages of mechanical failure, let alone total mechanical failure. The final choice of fibres must await complete optical and mechanical characterization at cryogenic temperatures, as is being conducted by researchers at the INO, AAO and GSFC/JPL.

The positioning device discussed in the remainder of this report could be used as a test bed for the evaluation of new fibre products, and thus would be a valuable contribution to the scientific community and to the progress of the NGST MOS project.

2.2. Piezo Electric Actuators

Piezo actuators were chosen for our conceptual design because they offer some unique advantages. Firstly, piezos are a solid-state ceramic which undergo a dimensional change (expansion) when a voltage is applied across it. This implies that the device has no inherent friction or wear associated with its operation. It requires no moving parts or lubrication, and is therefore straightforward to space-qualify. Secondly, as a result of the small scale motion, high resolution positioning is possible. Piezos are commonly used for optical alignment and sub-micron positioning. Next, unlike other actuators, piezos have already been demonstrated to work in cryogenic conditions. They do suffer from a decrease in stroke length at reduced temperatures, but otherwise retain acceptable performance [12] [13]. Finally, piezo actuators are a primary technology being studied for the adaptive optics aboard the NGST [14]. This means that significant research and development is already underway to develop piezo actuators for cryogenic, vacuum conditions.

For the proof of concept device, it was apparent that piezo actuators with a large stroke would be beneficial. Therefore, two commercially available devices with integrated motion amplification structures were studied. These products were the APA-100S from Cedrat Recherche, and the FPA-100 from Dynamic Structures and Materials. As shown below, these actuators utilize a flexible metal casing to amplify the motion of the piezo stack. Due to the geometry of the casing, the output of the piezo actually contracts (instead of expands) when the voltage is applied.

Cedrat Recherche SA,
AMA Department
Zirst, 38246 Meylan Cedex, France
Tel (33) (0)4 76 90 50 45,
Fax (33) (0)4 76 90 16 09
<http://www.cedrat-grenoble.fr/actuators/actua.htm>

(APA-100S Actuator)



Dynamic Structures and Materials, LLC
309 Williamson Square
Franklin, TN 37064
Tel: (615) 595-6665
Fax: (615) 595-6610
<http://www.dynamic-structures.com>

(FPA-100 Actuator)

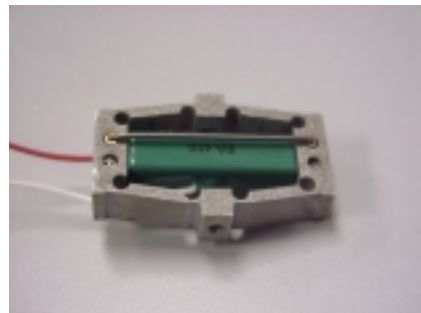


Figure 2.12. Possible cryogenic piezoelectric actuators.

2.2.1. Specifications and Power Consumption

Each of the two devices considered has a nominal stroke length of 100µm at room temperature. The APA-100S actuator has the more favorable performance specifications which are listed below. These reflect the assumed performance at 30K, where the stroke is reduced by approximately 50%-80% [13] [15].

APA-100S actuator	
Size	5 x 10 x 25 mm
Stroke (@ 30K, assumed)	20µm
Resolution	< 1µm
Voltage	200V
Capacitance	0.73µF
Blocked force	20N
Resonant frequency	1.6KHz
Response time	2ms

Using these specifications, it is possible to estimate the power consumption of each piezo based on the voltage, capacitance and frequency of operation. In the extreme scenario, a movable bar carrying the fibre bundles is required to translate across half the focal plane (90mm). By taking 20µm steps, this is equivalent to 4500 steps. If the motion is to be completed in 10 minutes, this would require an operating frequency of $f = 7.5\text{Hz}$. Since the piezo ceramic behaves like a capacitor, the power consumption of each piezo can then be calculated using the following formula:

$$P = V^2 (2\pi f) C$$

With the values quoted in the specifications and the calculated frequency f , the power consumption of each piezo is found to be $P = 1.38\text{W}$. It is important to note that this power is not all dissipated as heat at the focal plane. Indeed, the majority of it is dissipated as heat in the electronic amplifiers which control the piezos. These amplifiers will need to be located in the "warm" part of the satellite, away from the thermally sensitive instruments. There is, however, a small amount of heat dissipated by the piezos themselves at the focal plane. The amount depends on the dielectric loss of the piezo ceramic material. Fortunately, Cedrat Recherche has stated that this loss decreases sharply at low temperatures, and expects that a low-loss piezo material would only dissipate approximately 0.01W at the focal plane. This small amount of heat may need to be removed from the focal plane with a conductive or radiative cooling system. It should be noted that this heat is only generated when the piezo is active. In our slit mask design, the actuators are only active during reconfiguration, and are all inactive during exposure.

2.3. Safety and Redundancy

Since the NGST will be placed in orbit that prevents servicing missions, all components must be designed for maximum safety and redundancy. This means that in the event of equipment failure, the satellite can continue to function with the maximum capability possible. To address the issues of safety and redundancy, the conceptual design of the fibre manipulator includes several notable features.

2.3.1. Independent Movable Bars

Referring to Figure 1.1, the movable bars are arranged side by side in a linear arrangement on two sides of the focal plane. Each bar has its own set of guide posts and clutch piezos. In the event of a clutch piezo failure, the bar can no longer be reconfigured for observations, but will not interfere with the remaining bars. The clutch piezos can be designed such that if failure occurs, they will remain in either the clamped or unclamped state. It seems desirable to have one clutch nominally clamped when unpowered while the other is unclamped when unpowered. This would prevent binding of the carriage in the unlikely event that both clutches on a single movable bar failed.

2.3.2. Redundant Actuators

One of the most interesting aspects of this design is the use of redundant actuators. Although two *clutch* piezos are required for each movable bar, one is not restricted to use a single *actuator* piezo. In the minimal case, only one actuator is needed to move all the bars on one side of the focal plane. However, in practice, several actuators can be mounted in parallel for redundant operation. In this case, if one actuator piezo fails, another could take over the function of moving the bars. For example, our proof of concept device described in Section 3 incorporates two actuator piezos which can be operated individually or together.

The key to the feasibility of this redundancy concept is to ensure that a failed actuator can not impede the performance of the remaining active devices. The conceptual design incorporates a special type of connection which achieves this goal. When the actuator is activated it contracts and pulls the entire movable carriage towards the focal plane. When the voltage is removed, the spring force in the flexures returns the carriage to its original position. Although the actuators are capable of pulling on the carriage, they are not rigidly attached. If an actuator fails, the carriage would be translated by the other actuator piezos and a gap would simply form between the malfunctioned piezo and the carriage. In this way, the failed actuator would become mechanically uncoupled from the system.

2.3.3. Other Technologies

It is worth noting that piezo actuators represent a safe, conventional technology for actuating the fibre manipulator. Although other options exist (e.g. electric motors with ball screws) these devices have friction, wear and often require lubrication. Their long-term performance at cryogenic temperatures may be questionable.

Other options such as MEMS devices being studied in the USA and at Simon Fraser University (SFU) utilize a comparatively exotic technology which is unproven at cryogenic temperatures. In the concept being pursued at SFU, micro shutters are opened by thermal actuators etched in a silicon substrate. These actuators move by using the differential expansion of two parts heated by an electric current. The researchers at SFU have noted that during operation, the silicon substrate became "red hot" due to the prolonged high frequency operation. This heat generation could have obvious detrimental effects on both the mechanical components and on the quality of observations. Compared to MEMS solutions, a mechanical piezo driven manipulator is a safe, conventional device.

2.4. Additional Options

During the development of the conceptual design, it became evident that many additional options could be incorporated to improve the performance of the device. Many of the options presented here have not yet been explored in detail and are left for further research.

2.4.1. Image Slicer

One interesting concept is to incorporate an image slicer into the same package as the fibre positioner. It has been proposed that the image slicer could be mounted in the centre of the focal plane, between the movable bars. This arrangement would naturally restrict the motion of the fibre slitlets in the central region, but is an acceptable trade-off. A preliminary design incorporating the fibre slitlets and image slicer is shown in Figure 2.13, created by EMS Technologies in Ottawa.

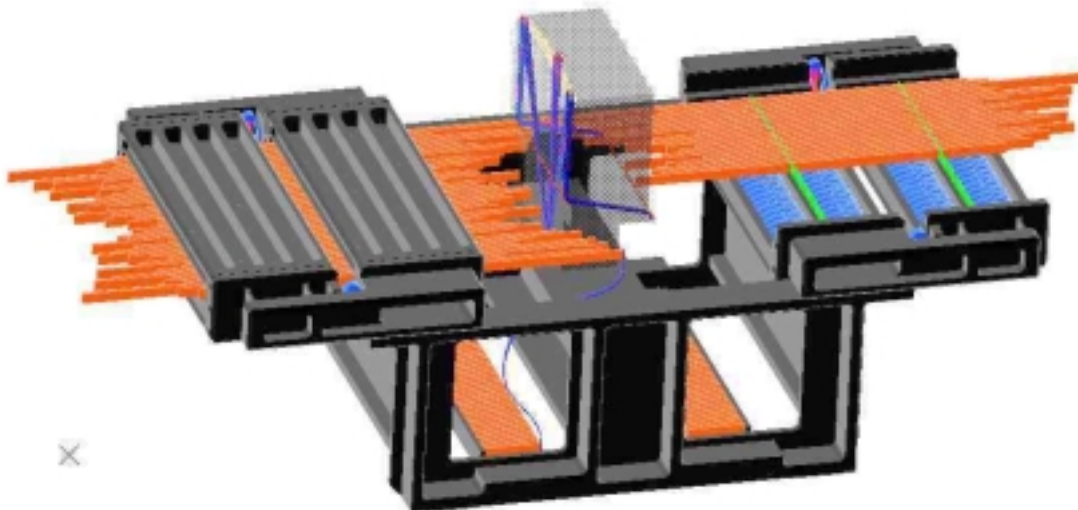


Figure 2.13. NGST MOS fibre manipulator with additional image slicer (courtesy EMS Technologies)

2.4.2. Optical Position Feedback

To achieve high accuracy positioning of the fibre slitlets, some form of position sensing would be required. Several methods of position sensing have been put forward, for example, using the instrument's CCD detector or installing an optical feedback device such as a linear encoder. A linear encoder uses an LED and a photo-transistor along with a strip of opaque material containing thin slits at regular intervals. The strip moves between the LED and transistor and generates a square-wave signal at the transistor. By counting the number of pulses of the wave, the exact position of the bar can be determined. This type of device could be easily attached to the back end of each movable bar.

2.4.3. Multiple Fibre Sizes

It is not necessary to have only one fibre slitlet at the end of the movable bar. Multiple slitlets could be arranged which have different fibre sizes, or are optimized for different wavelengths of light. In this way, the device could be used for limited "3D" observations which combine spatial and spectral information. Since the fibres can be reformatted at the entrance to the spectrograph, multiple slitlets can be used to extend the performance of the device. A movable bar with two slitlets (and two rows of fibres) is shown schematically in Figure 2.14.

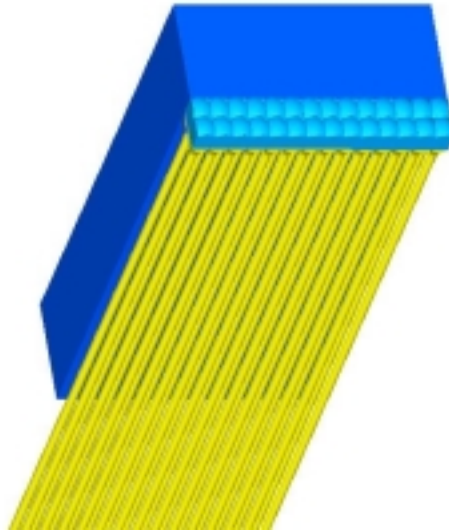


Figure 2.14. Movable bar with two fibre slitlets

2.4.4. Long-Stroke Operation

One drawback with the current design is that the piezo actuators must be activated in a cyclic fashion for the duration of the movable bar's motion. This may require thousands of cycles for a single reconfiguration and contributes to increased heat production and decreased lifetime of the piezos. One solution to this problem is to retain

the clutch piezos in their current configuration, but replace the actuator piezos with a long-stroke linear actuator such as a stepper motor and ball screw. Also possible in this application are the Burleigh inchworm actuators and the New Focus Pico motor, both of which are being considered for actuation of the NGST's deployable mirror. With this arrangement, the movable carriage could be translated over the maximum required stroke (90mm), and would require only one cycle. During the motion, the clutch piezos would clamp or unclamp at the required time to position the movable bars. Since only one large step is taken, each clutch piezo must operate for only one cycle per reconfiguration. The obvious benefits are decreased heat production and increased actuator life.

3. Proof of Concept Device

In order to test the fibre manipulator concept, a proof of concept device was designed and built. Due to budget and time constraints, this device is capable of actuating only two movable bars without fibres. In most other respects, though, the device was built to reflect the design for the complete slit mask. Following are photographs of the device showing various components and the final assembly.

The principle differences between the conceptual design and the proof of concept device as constructed are: only two movable bars, the supplier of the piezos, and the arrangement of the clutch piezos. As mentioned before, time and budget constraints limited the number of movable bars to two. A third bar was included (as seen in the following figures) to demonstrate issues such as spacing and guiding, but this bar is not actuated. This also means that the movable bars were only placed on one side of the focal plane. In the actual design, the bars would move across the focal plane from two sides.

The piezo actuators chosen for this design were the FPA-100 series supplied by Dynamic Structures and Materials. The APA-100S actuators from Cedrat Recherche were preferred due to slightly better performance characteristics and an overall smaller size, but they could not be delivered within the time constraints of this project. One result of using commercially available actuators is that the clutch piezos were greater than 3mm in width. This meant that the clutches had to be mounted with an orientation of 90° to the desired direction. For a device with only two movable bars, this did not pose a problem, but for the final design the issue of packing of piezos must be addressed. In all other respects, the proof of concept device was built to closely reflect the final design.

3.1. Component Photographs

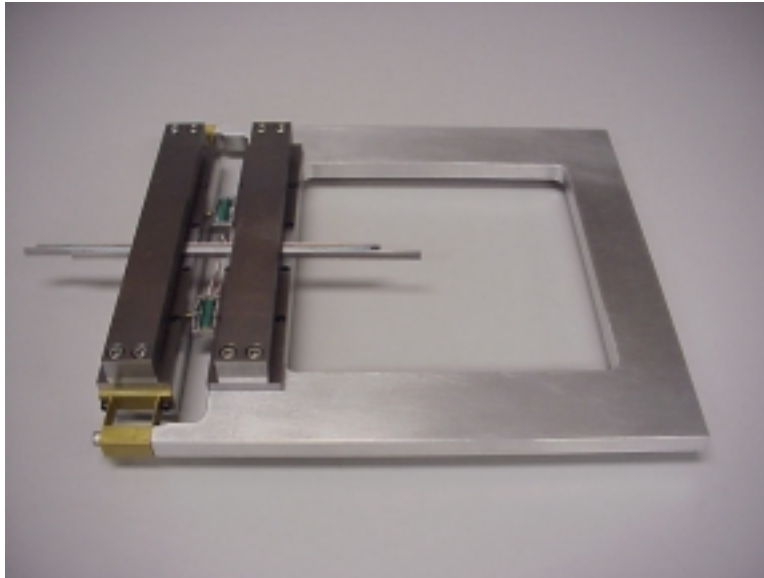


Figure 3.1. Final assembly of fibre manipulator.

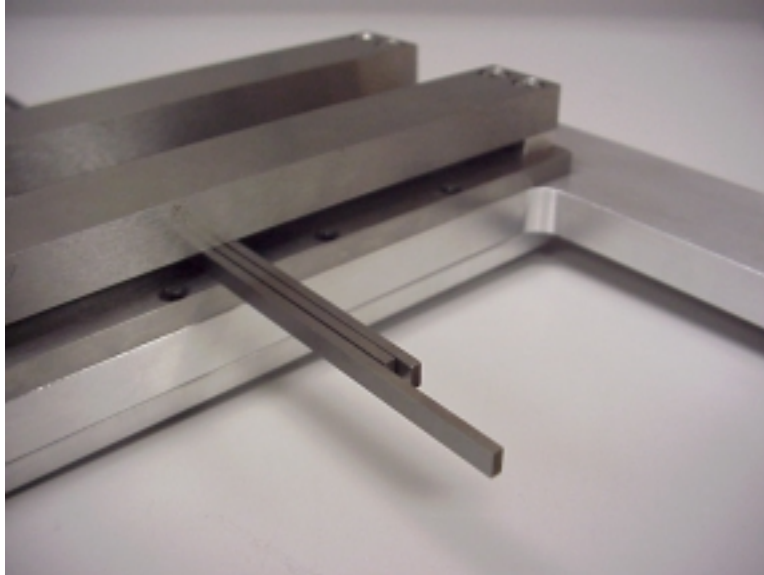


Figure 3.2. Assembled device showing three movable bars.

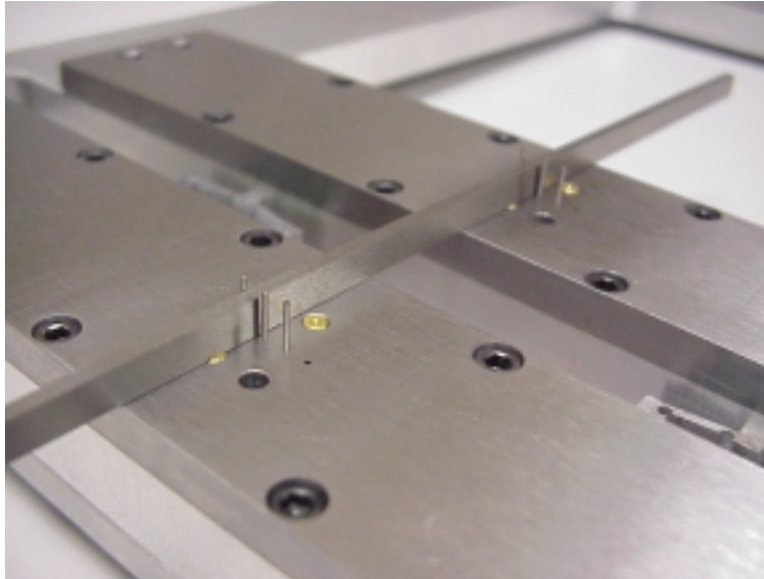


Figure 3.3. Movable bar, guide posts and clutch posts.

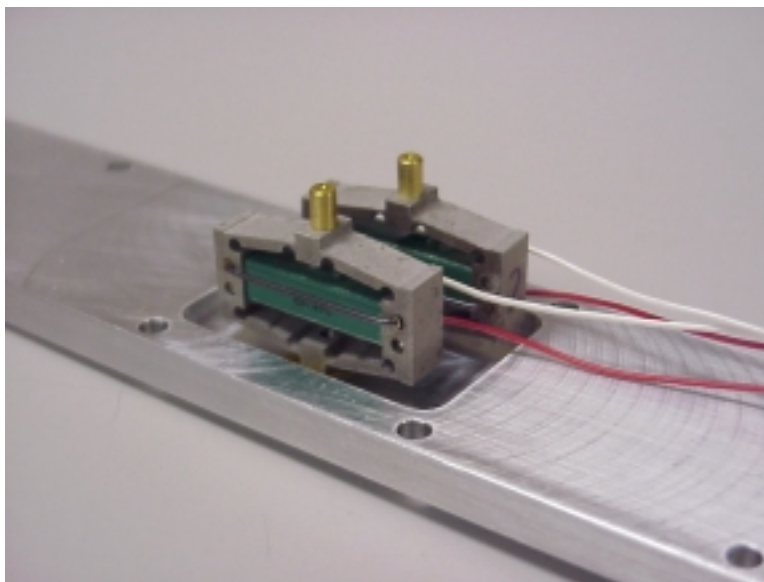


Figure 3.4. Clutch piezos on mounting plate.

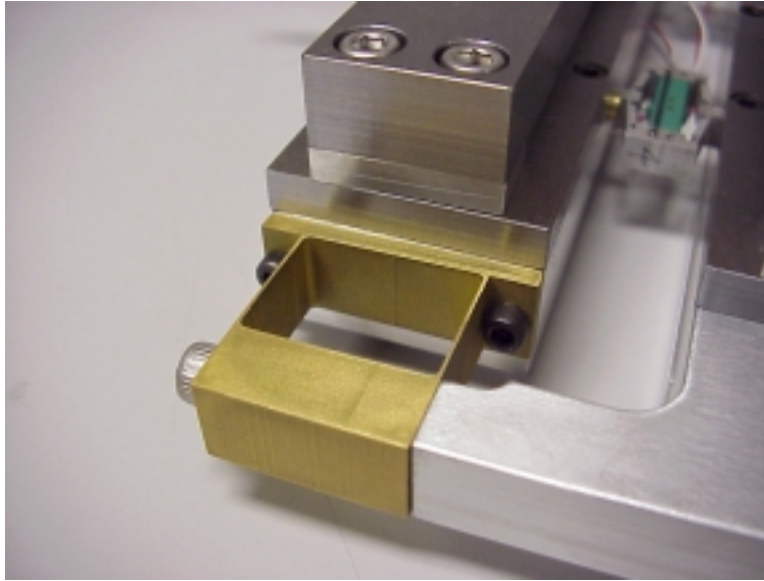


Figure 3.5. Movable carriage mounted on flexure hinges.

3. 2. Piezoelectric Controllers

In order to control the six DSM actuators of the prototype manipulator, six independent amplifiers were constructed. To generate the fixed increments of motion of the slider bars it was only necessary to run the actuators between two states: an *on* state corresponding to delivery of 150V by the amplifiers, and an *off* state which corresponded to a 0V signal. The amplifier inputs were 0V or 5V signals supplied by the digital channels of a parallel port of a standard personal computer. Two types of amplifiers were constructed: those dedicated to the control of the clutching piezos, and two amplifiers which were responsible for controlling the actuator piezos.

3.2.1. Controlling the Clutching Actuators

The prototype amplifiers allow for adjustments to be made to the peak voltage which they deliver to the clutching piezos. Dynamic Structures and Materials has supplied calibration curves, located in Appendix A, which describe the extension generated by each actuator during a 20Hz voltage loading cycle. These plots illustrate how there is variation in the extension of each actuator. In order to accommodate these variations in the performance of the six actuators, each amplifier circuit is equipped with a 50k Ω , 10 turn potentiometer which provides $\pm 10V$ at the piezo input voltage. This allows for the differences in the performance of the actuators to be accounted for. This mode of adjustment also allows for very fine tuning of the stroke of the clutching actuators to ensure that the clamped and unclamped states are achieved. Although we did not need this adjustment during our operation of the prototype manipulator, it could prove very useful in situations where thermal expansion must be accounted for.

3.2.2. Control of Carriage Actuators

Although the amplifiers we have constructed deliver a square wave signal, the capacitive nature of the actuators result in a rise time of 5-8ms. In order to ensure smooth carriage motion, the ability to adjust this rise time has been provided in the amplifiers that are dedicated to the carriage actuation.

Simulations of the carriage motion developed using Simulink have shown that as the carriage moves into a new position, it will oscillate about that position at a frequency much higher than the frequency of the control signal. The frequency of this oscillation is directly related to the relatively high stiffnesses (10^5N/m) of the structures which support the carriage: the set of translational flexures, and the actuator which drives the carriage motion. The simulations have also shown that the magnitude of these higher frequency oscillations can be decreased by allowing for longer rise times in the application of the "on" or 150V control signal. This degree of freedom is accomplished with an additional $50\text{k}\Omega$, 10 turn potentiometer.

3.2.3. Frequency Issues

Referring to the table of constraints presented in Section 1, the sequencing between the "on" and "off" states of the actuators which drive the carriage must be completed at 1-10 Hz. This allows for the breadth of the focal plane to be easily covered in the requisite 20min. In this range of frequencies, the piezoelectric actuators are being driven well below their bandwidth of normal operation ($>200\text{Hz}$). This allows us to make use of two advantages. Firstly, the input waveform delivered to the actuator by the amplifier can be very sharp. This allows us to deliver a square wave form with a 150V peak to the actuators, without risking the decreased life expectancy that is associated with the use of this type of input at higher frequencies. At such low frequencies, we are also able to operate over the entire 150V operating range with a constant bias. At higher frequency operation it is the manufacturer's suggestion that the 150V range of the actuators be accomplished between -20V and 130V. The lower overall voltage in this range prevents additional heat dissipation within the actuator and helps increase actuator lifetime.

3.3. Performance

Once the mechanical parts were assembled, all electrical connections were made and the device was tested. As expected, the manipulator was able to translate two movable bars across one-half of the focal plane. Some simple testing led to the following observations:

Length of a single step	50 μm
Max. frequency (with existing PC)	5 Hz
Max. time to reconfigure (90mm stroke)	6.5 min

It was noted that positioning accuracy was only 1-2 mm, which is larger than expected. There are two main causes for this. First, the movable bar may "miss a step" from time to time due to excessive friction in the sliding surfaces. Alternately, the stroke length setting in the driving software may be slightly inaccurate. This would cause an incorrect calculation of the number of steps required to complete the motion.

Regardless of the reason, this observation points to the need for some type of position sensing and feedback control.

Based on the performance of the manipulator, it is felt that the concept of using piezo actuators to manipulate multiple fibre slitlets has been proven. Additional work should focus on cryogenic operation, positioning accuracy and thermal emissions.

4. Conclusions

A reconfigurable slit mask device has been designed and proof-of-concept constructed in the Space and Subsea Robotics Laboratory at the University of Victoria. The device uses fibre optic bundles to form slits in the focal plane for the NGST MOS. Positioning of fibres is achieved by means of two types of piezo electric actuators---one to clutch the movable bars carrying the fibres and the other to actuate the supporting carriage. A survey of existing fibre optics technologies revealed favourable findings in terms of availability of fibres capable of NIR transmission. As well, research on fibre optics performance at cryogenic temperatures is progressing rapidly.

The performance of the design was demonstrated with a two-slit mask proof of concept device. The device functioned successfully although it did not meet the positioning accuracy specifications due to lack of position feedback. The design of the complete slit mask incorporates a number of advantages, such as redundant actuation, possibility of using position feedback and different slit sizes to further improve MOS functionality.

5. Recommendations

There is still substantial work to be done to ascertain whether the conceptual design presented here will be a viable solution for the NGST MOS slit mask. First and foremost, since the design inherently assumes the existence of appropriate optical fibres, such fibres must be identified. Since a number of research groups and companies have already performed work in this area, it would be advantageous to contact them, perhaps form alliances with them, and obtain any quantitative data they may have. Once that is done, experimental testing of candidate fibres at cryogenic temperatures should be performed to support and complement any data obtained. In particular, the following properties must be quantified as being satisfactory for the purpose of the NGST slit mask: (a) mechanical strength, bend radius, stiffness, ductility, and fatigue life, and (b) optical transmission, focal ratio degradation, and numerical aperture. Methods for mounting the fibres on the rod ends without inducing thermal stresses at cryogenic temperatures must also be identified, as well as the design and construction of lenslets for channeling the light at the fibre inlets.

The design of the fibre positioner presented here is less crucial because, even if it turns out not to be viable, another approach could likely be proposed for this function. Nevertheless, assuming that the conceptual design presented here does form the basis for the final selected design, a number of items still remain to be investigated. First and foremost, the adequacy of piezo-electric actuators for operation at cryogenic temperatures must be ascertained. It is well known that the stroke of such actuators is reduced, but more quantitative data must be obtained for the specific actuators being considered, at 30 K. As well, the heat dissipation of these actuators, in the focal plane, must be quantified. It would likely be desirable to enlist one or more of the piezo manufacturers to custom-design an integrated actuator/flexure for this application. Hopefully, the actuators could be made more compact to improve the packing efficiency in the final design. As well, the amplifier and control circuitry should be redesigned to allow more accurate positioning of the actuators (as opposed to the on/off control used in our proof-of-concept device), though this is expected to be straightforward. Some means of sensing the position of the bars must also be devised to allow closed loop control of the bar positioning.

Further work needs to be done on the remainder of the positioning device for operation at cryogenic temperatures---in particular, choosing and sizing of materials for the frame, rods and flexures. Some analysis should also be performed to identify potential vibration problems of the rods both during operation and during launch. Finally, if the idea proves attractive, further work could also be done on the incorporation of an image slicer into the overall design.

6. References

- [1] B. Buckham, J.A. Carretero, D. Erickson, M. Nahon, and I. Sharf, *NGST Slit Mask Design Study*, Mechanical Engineering Dept., University of Victoria, Technical Report, January 1999.
- [2] K.H. Levin, D.C. Tran, and R. Mossadegh, *Properties and applications of infrared fibre optics*, Astronomical Society of the Pacific, Vol.3, pp.23-25, 1988.
- [3] K.H. Levin, D.C. Tran, and E. Kindler, *Infrared fibre arrays for low background infrared astronomy*, Astronomical Society of the Pacific, Vol.37, pp.295-309, 1993.
- [4] <http://huey.jpl.nasa.gov/~spravdo/circle.html>
- [5] K. Timmerhaus and T. Flynn, *Cryogenic Process Engineering*, Plenum Press, New York, 1989.
- [6] R.P. Reed and A.F. Clark, *Materials at Low Temperatures*, American Society for Metals, Metals Park, OH, 1983.
- [7] R. Dallier, J. Baudrand, and J.G. Cuby, *Near IR fiber spectroscopy: First results*, Astronomical Society of the Pacific, Vol.37, pp.310-320, 1993.
- [8] L.W. Ramsey, *Focal ratio degradation in optical fibres of astronomical interest*, Astronomical Society of the Pacific, Vol.3, pp.26-39, 1988.
- [9] M. Tecza and N. Thatte, *Sinfoni: a high-resolution near-infrared imaging spectrometer for the vlt*, Astronomical Society of the Pacific, Vol.152, pp.271-281, 1998.
- [10] G.W. Nelson, *Introduction to fibre optics*, Astronomical Society of the Pacific, Vol.3, pp.3-22, 1988.
- [11] F. Piche, I.R. Parry, K. Ennico, R.S. Ellis, P.J. Mackay, D. Craig and R.G. McMahon, COHSI: *The Cambridge OH Suppression Instrument*, Proceedings of SPIE, Vol. 2871, pp. 1332-1341, 1997.
- [12] <http://ngst.gsfc.nasa.gov/Hardware/text/ActuatorActivities.html>
- [13] <http://ngst.gsfc.nasa.gov/Hardware/meetings/techchal2.html>
- [14] NASA awards contracts for the Next-Generation Space Telescope, news release no. 98-014. Technical Report, March 24 1998.
- [15] Editors, *The New Melles Griot Nanopositioning Guide*, Melles Griot, pp. 1-1 to 3-11, 1993.

Appendix A: Piezo Calibration Curves

Part Number: FPA-100 UVIC 1

Calibration Data: 21-Jul-99

Calibration by: M. Samuelson

Actuator mass: 7.70g

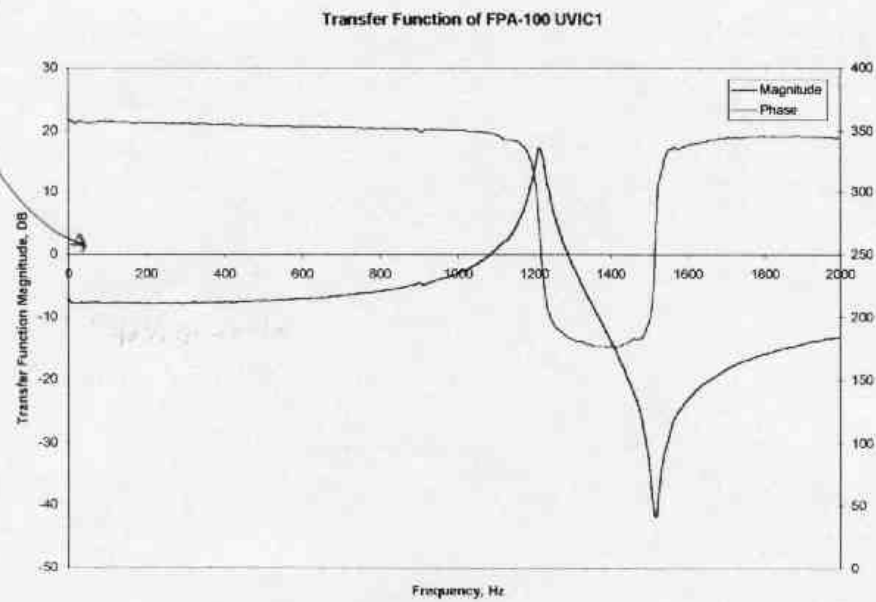
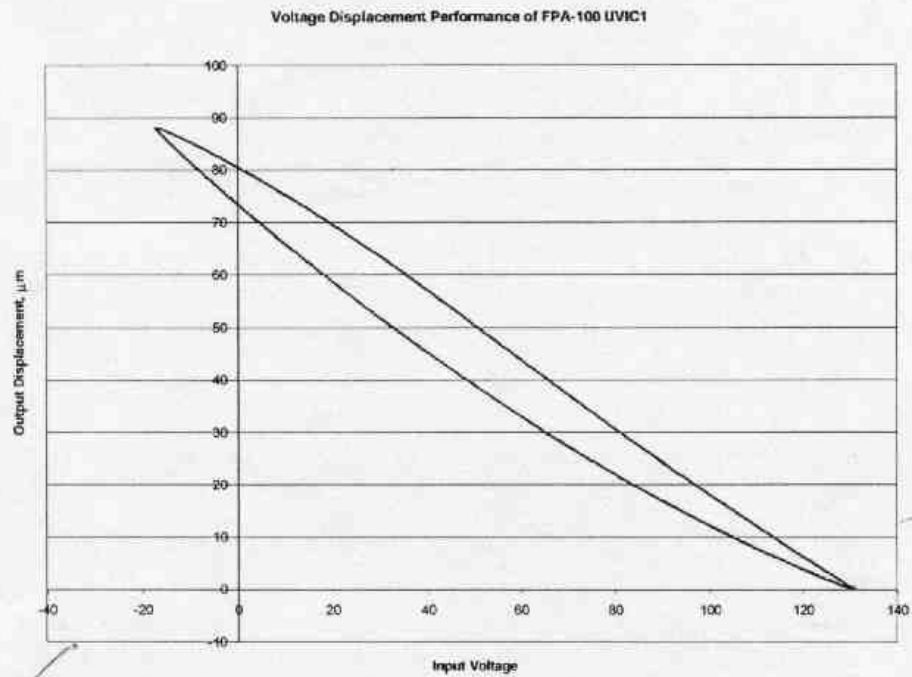


Figure A.1. Piezo 1 calibration curve

Part Number: FPA-100 UVIC 2
Calibration Data: 21-Jul-99
Calibration by: M. Samuelson
Actuator mass: 7.65g

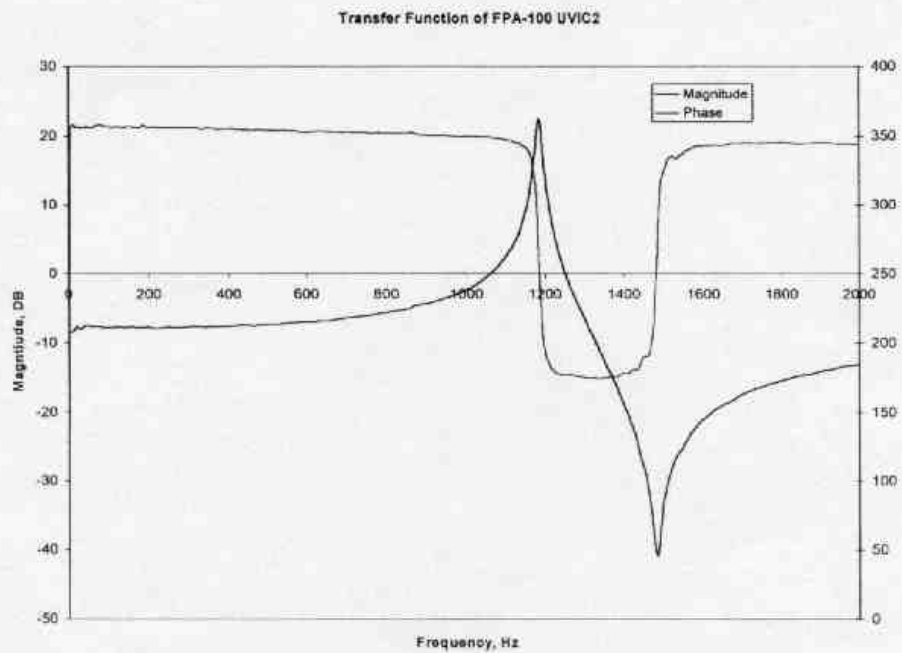
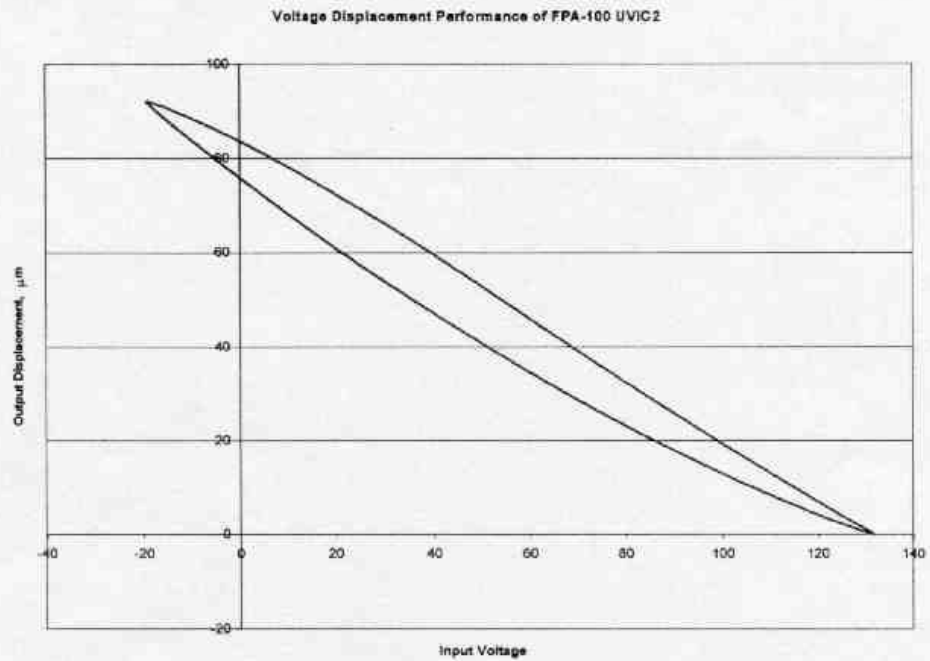


Figure A.2. Piezo 2 calibration curve

Part Number: FPA-100 UVIC 3
Calibration Data: 21-Jul-99
Calibration by: M. Samuelson
Actuator mass: 7.70g

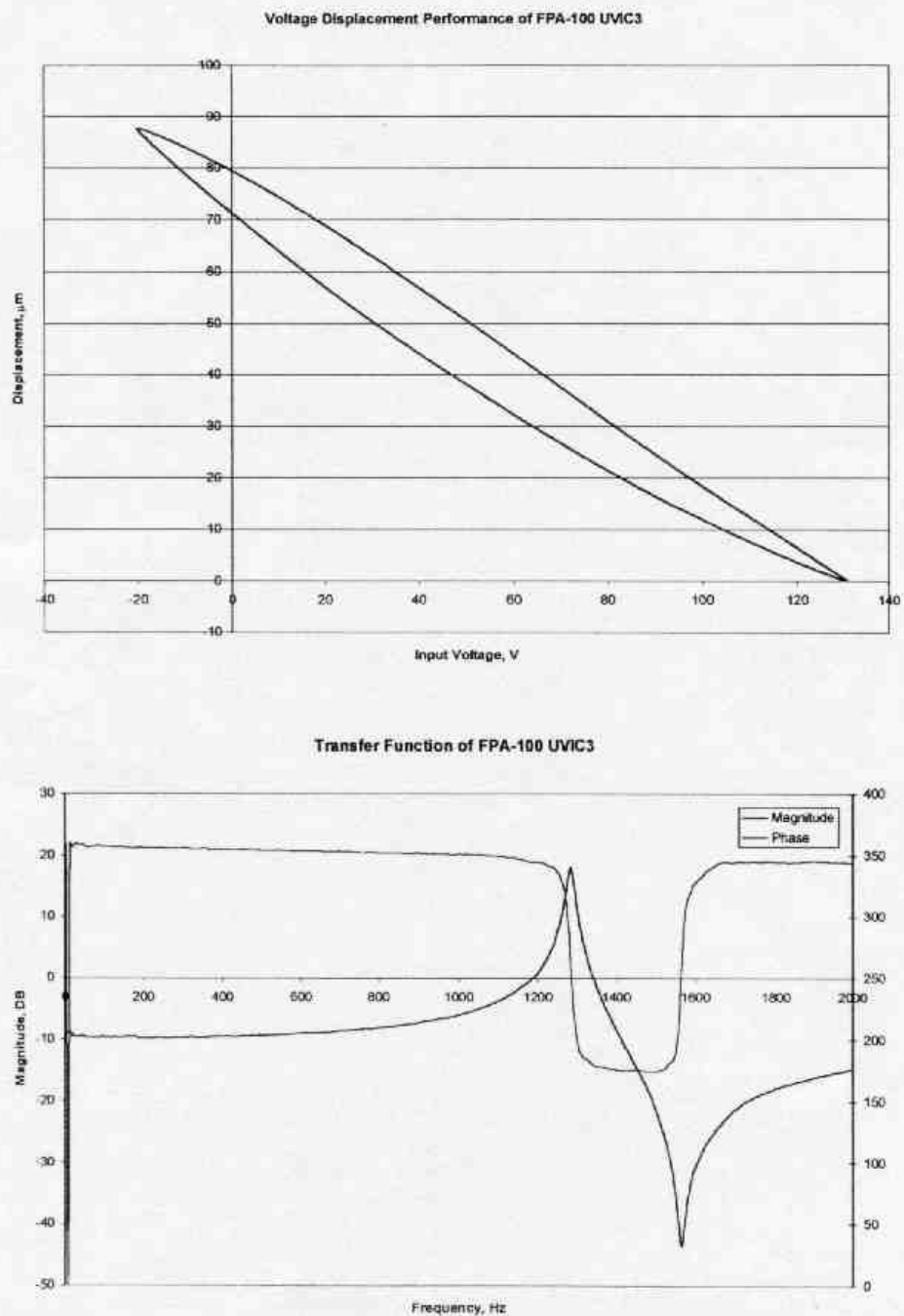


Figure A.3. Piezo 3 calibration curve

Part Number: FPA-100 UVIC 4
Calibration Data: 21-Jul-99
Calibration by: M. Samuelson
Actuator mass: 7.65g

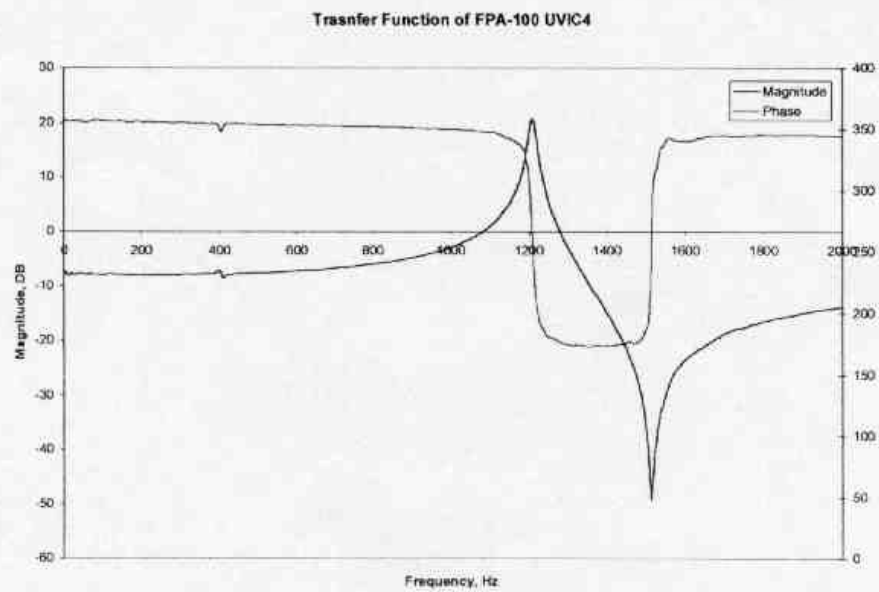
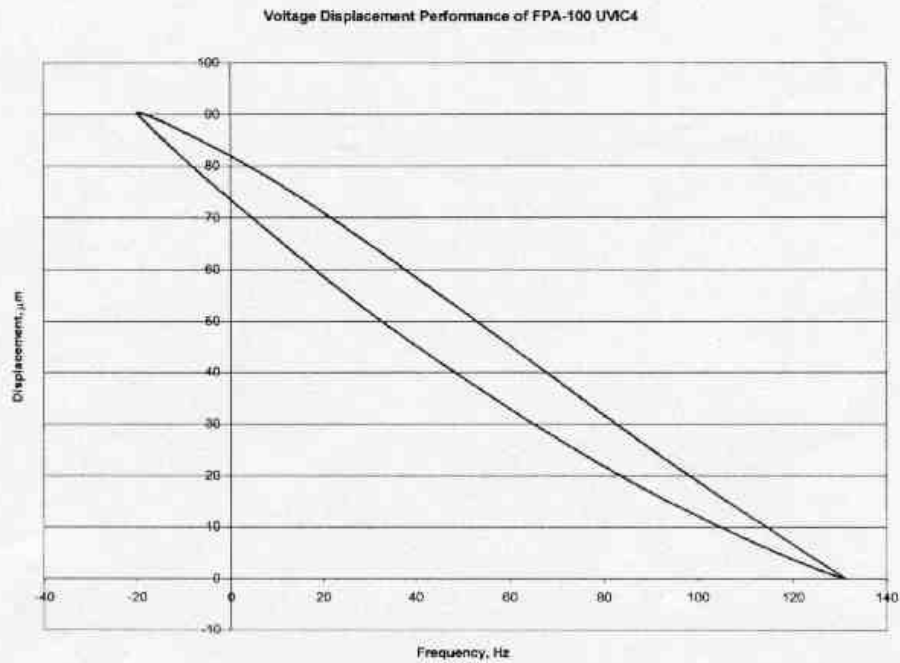


Figure A.4. Piezo 4 calibration curve

Part Number: FPA-100 UVIC 5
Calibration Data: 21-Jul-99
Calibration by: M. Samuelson
Actuator mass: 7.65g

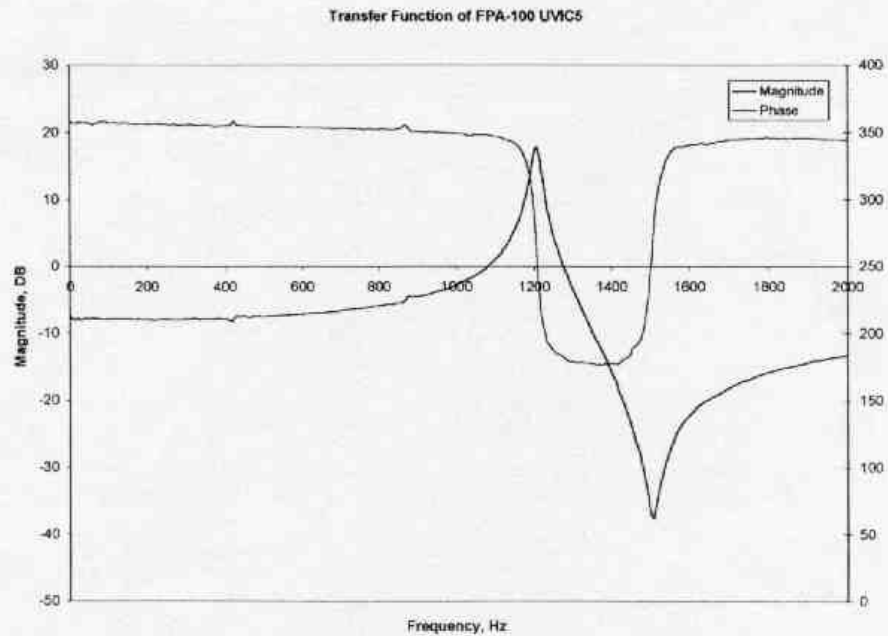
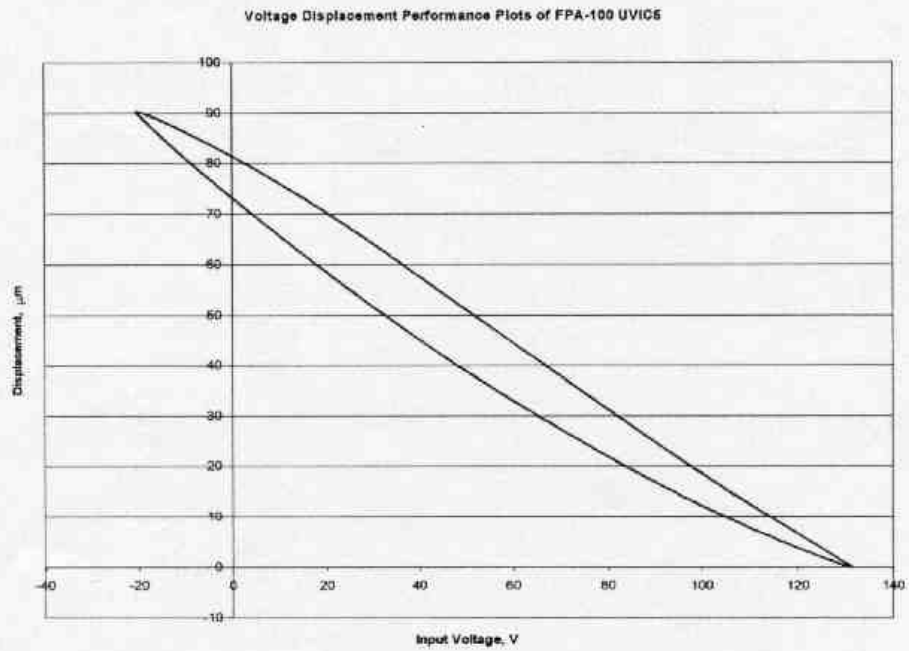


Figure A.5. Piezo 5 calibration curve

Part Number: FPA-100 UVIC 6
Calibration Data: 21-Jul-99
Calibration by: M. Samuelson
Actuator mass: 7.65g

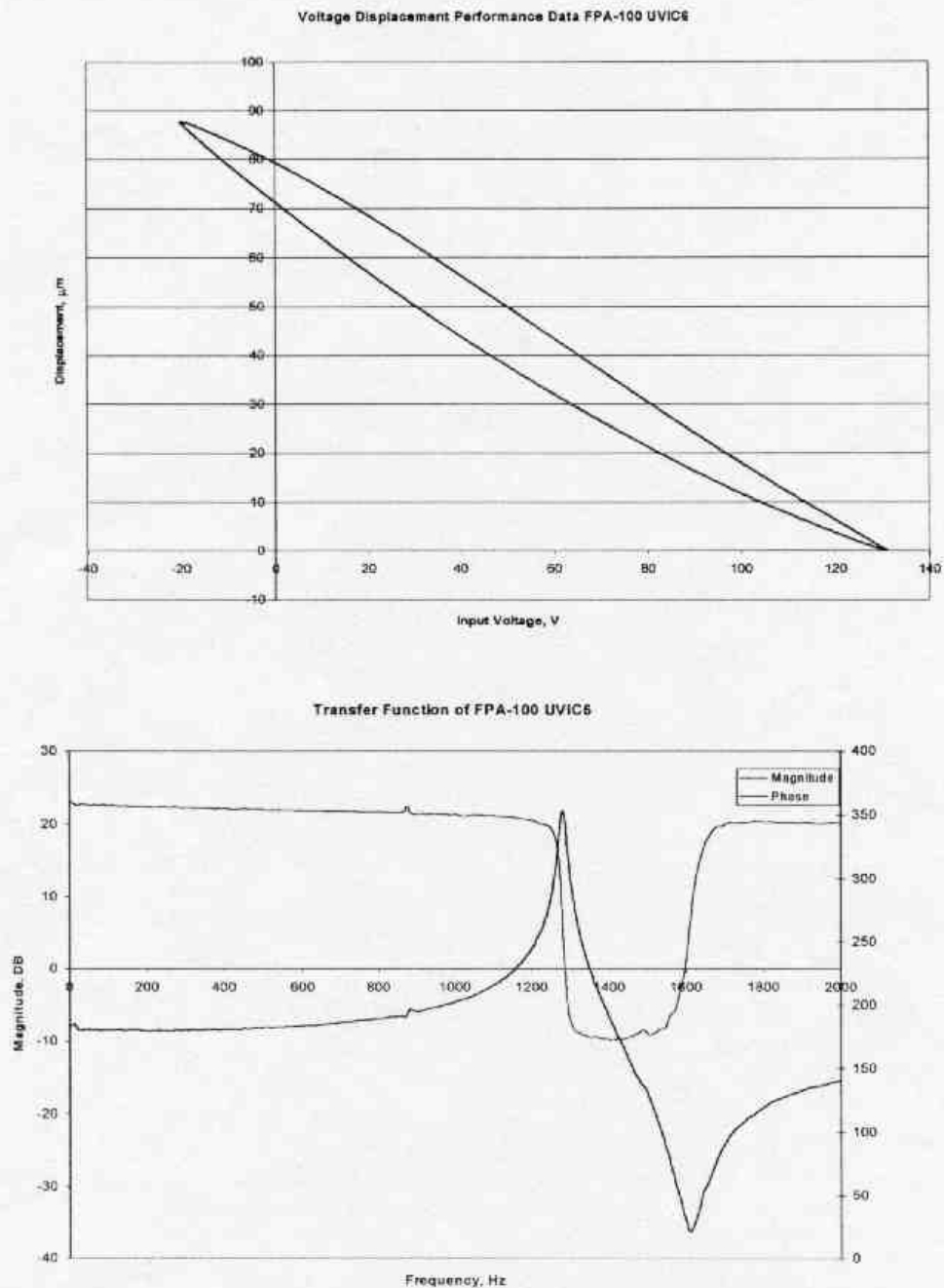


Figure A.6. Piezo 6 calibration curve

Part Number: FPA-100 UVIC 7
Calibration Data: 21-Jul-99
Calibration by: M. Samuelson
Actuator mass: 7.65g

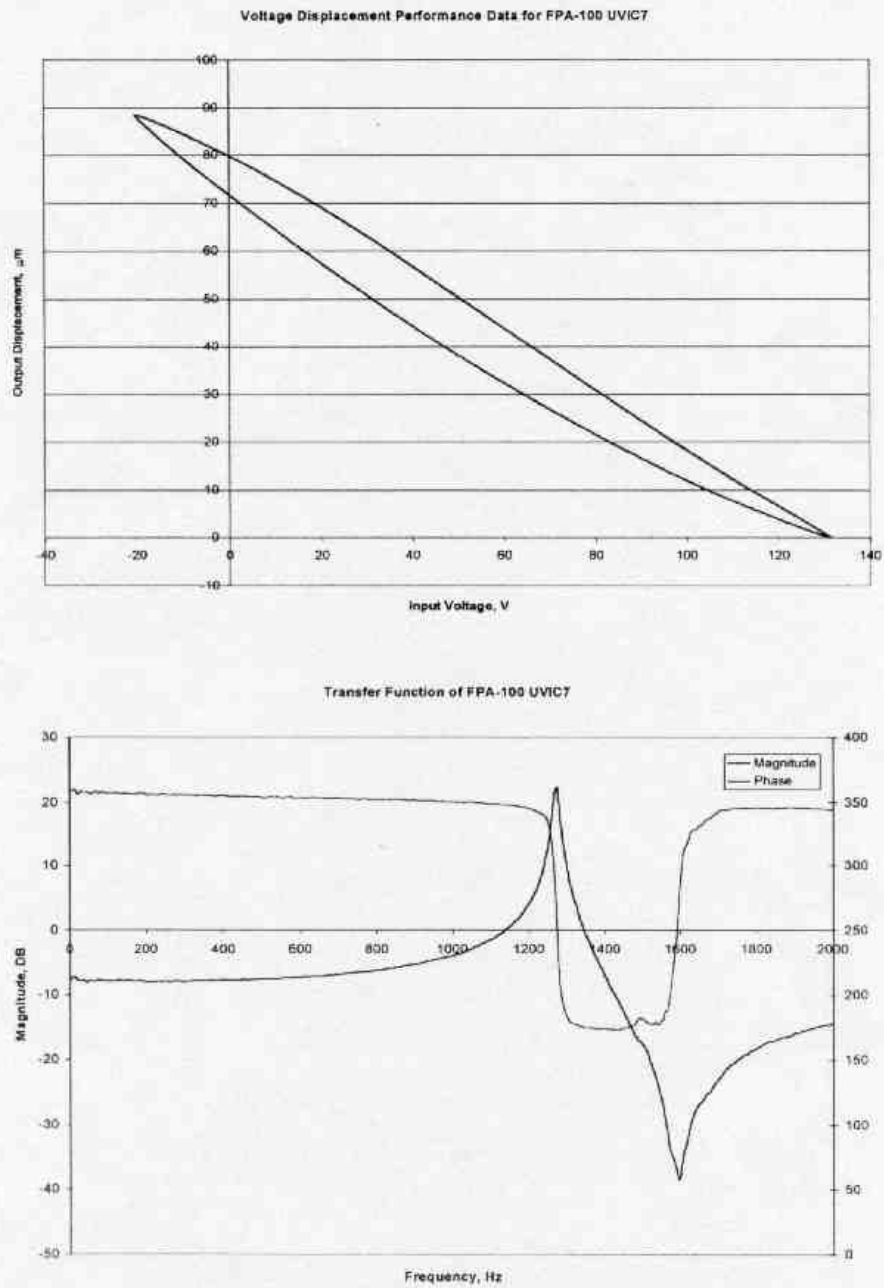


Figure A.7. Piezo 7 calibration curve

Appendix B: Computer Control System

The fibre manipulator is controlled using a PC running Windows 95/98. This computer is connected to the piezo amplifiers via the parallel port. Unfortunately, due to restricted access to the parallel port under WinNT, the control software does not run with that operating system. To simplify use, a graphical user interface was developed to specify the desired motion and customize the settings.

Running the program

- In Windows 95/98, open the *Start - Programs* menu.
- Click on the *Run NGST Prototype* link. A dialog box will appear as shown in Figure B.1.
- To insert or reposition the slider bars by hand, click on the *Settings* button.
- A second dialog box will appear as shown in Figure B.2.
- Click on the Clutch 1, Clutch 2, Clutch 3 and Clutch 4 boxes to turn on (retract) the clutch piezos. The slider bars should now move freely into position.
- Click on *Close*.
- To activate the device, drag the two trackbars to the desired locations and press *Move*.

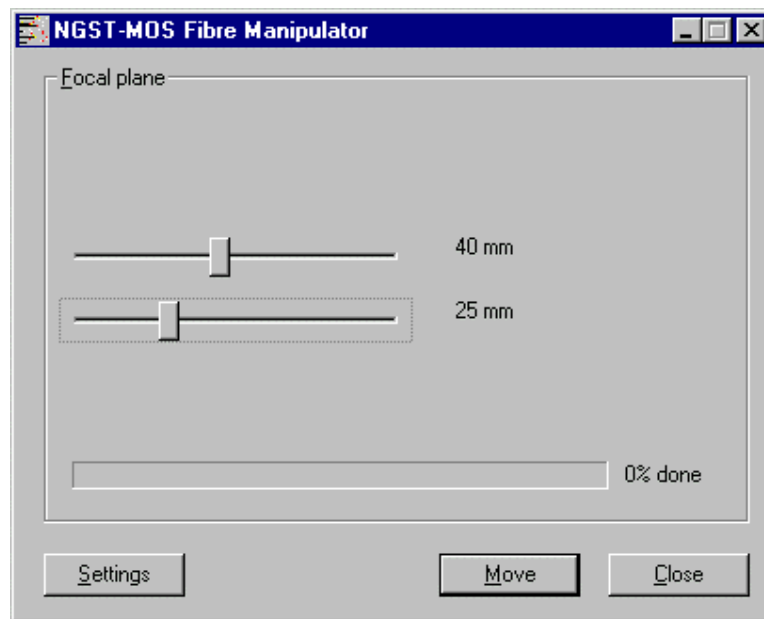


Figure B.1. Control program main window

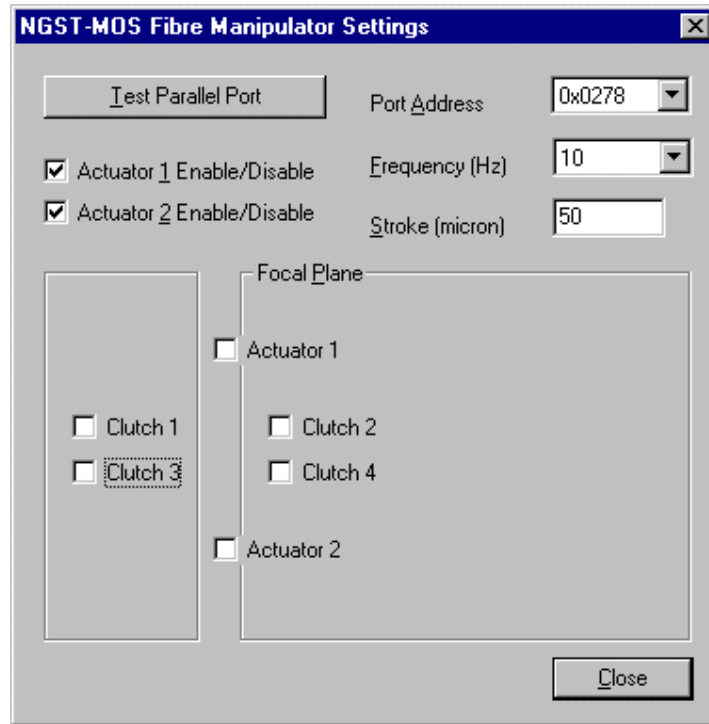


Figure B.2. Settings window

Software Troubleshooting

If nothing happens when you press *Move*, there may be several causes:

- The cable connections are not fully contacting. Verify that all cables are fully connected.
- The power is not on. Plug in amplifier and turn on power switch.
- The parallel port setting is not correct. Look in the *Windows Control Panel* under *System, Device Manager* for a folder called *Ports*. Expand this folder, highlight *LPT1* and press *Properties* then *Resources*. Take note of the input/output range. It should resemble something like *0x0378*. Next open the NGST controller program and press the *Settings* button. In the *Port Address* list box, highlight the parallel port I/O address that was listed in the *Control Panel*. Close the *Settings* dialog box and re-try the program.

CAUTION - The *Test Parallel Port* button is meant to test the connections and address settings of the software. However, the input impedance of the parallel port has not yet been measured. If the impedance is very low, then pressing the *Test Parallel Port* button may cause the port to short circuit. For the present, **DO NOT USE** this feature.

Customizing the motion

The Settings dialog box allows the user to change many of the settings used in the control program such as stroke length, frequency and number of actuators used.

- To change the frequency, click on the down arrow and select one of the options. Depending on the speed of the computer, it may not be possible to achieve some of the higher frequency motions.
- To change the stroke length used in the program, click in the edit box and type the new value (in microns). This value should be edited if the observed motion is different from the desired motion.
- The actuator enable/disable feature can be used to turn off or on one of the actuators and demonstrate the redundant operation. The program only permits one actuator to be turned off at a time.

As mentioned above, DO NOT USE the *Test Parallel Port* button. Until the input impedance of the parallel port is determined, this feature should not be used or else damage to the computer may result.

SURFACE MICROMACHINED RECONFIGURABLE MULTI-SLIT MASK

S.Bakshi, M.Parameswaran, M.Syrzycki

Simon Fraser University, Burnaby, British Columbia, V5A 1S6

Tel:(604)291-4971 Fax:(604)291-4951 Email:param@cs.sfu.ca

September 23, 1999

A Progress Report Submitted to the
National Research Council,
Victoria, British Columbia, V8X 4M6

**School of Engineering Science,
Simon Fraser University,
Burnaby, BC, V5A 1S6
Canada**

TABLE OF CONTENTS

1.	Abstract	3
2.	Introduction	4
3.	Design	7
4.	Test Results	12
5.	Ongoing Work	14
6.	Conclusion	15
7.	Acknowledgments	15
8.	References	16

ABSTRACT

The concept of an electromechanically reconfigurable multi-slit mask has been proposed using a 3-poly surface micromachining technology. The fabricated prototype device consists of a 300 μm by 1.2mm shutter along with a thermal actuator based stepper motor. The stepper motor has a 10 μm stroke and consumes 300mW per cycle of operation. A flange-type guide rail design has been incorporated in the shutter to permit linear translation in only one axis.

INTRODUCTION

The general principle of the reconfigurable slit mask is illustrated in Figure 1. Each slit unit consists of a physical opening (slit) along with a sliding plate (shutter). An actuation mechanism (linear stepper motor) moves the plate such that the opening can be covered or uncovered electromechanically.

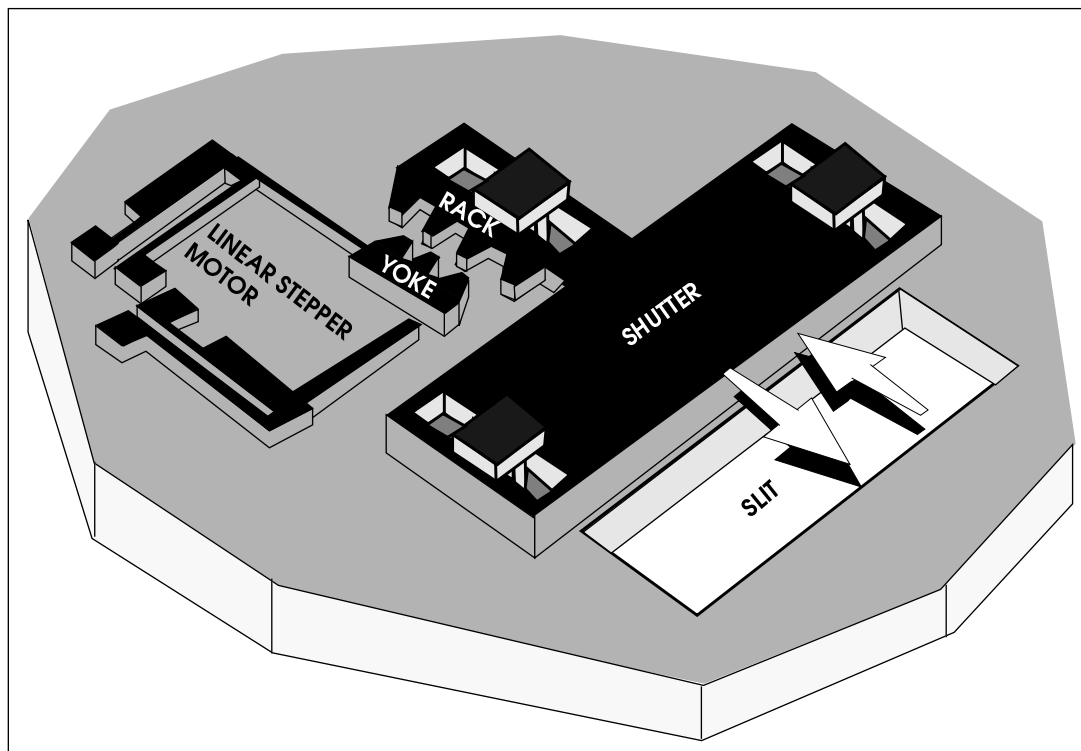


Figure 1. Reconfigurable slit mask layout

A two dimensional array of this design shown in Figure 2, would form a reconfigurable multi-slit mask for MOS studies.

Each shutter is addressed by row/column decoding techniques using integrated diffusion type diodes. Diodes act like switches and are turned on when a forward biasing voltage is applied across them. As is shown in Figure 3, diodes connected in series with the actuators are connected between each overlapping row and column line. By powering and grounding the appropriate lines,

the required actuators can be turned on or off.

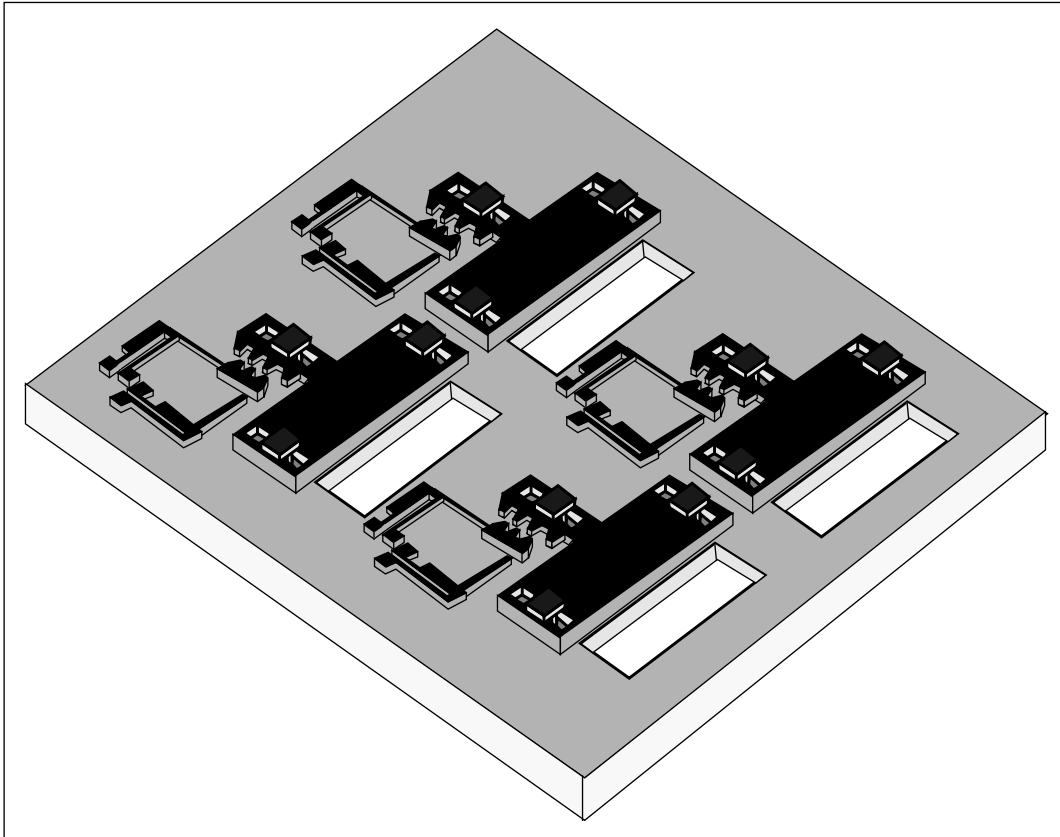


Figure 2. Multi-slit mask

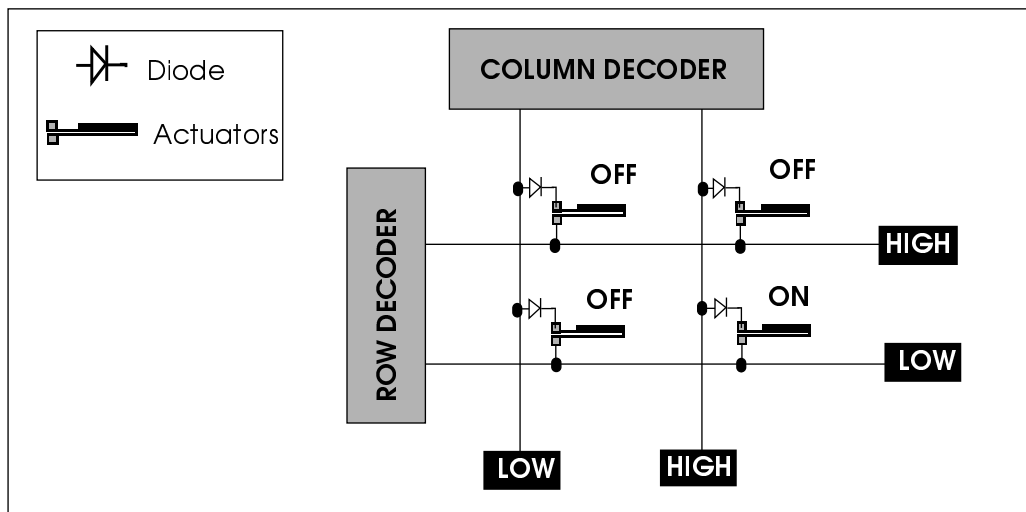


Figure 3. Row/Column addressing of individual actuators

The row/column decoding technique permit one set of actuators to be turned on at a time. Hence, the total time taken to open/close multiple shutters is a sum of the time taken by individual shutters.

Until now, we have designed and tested individual shutters with a built-in actuation mechanism. The following sections of this report discuss the design and test results of the work we have performed so far.

DESIGN

The design of the shutter and actuation mechanism is based on a 3 polysilicon layer surface micromachining technology [1]. The design is a combination of a sliding shutter with an actuation rack and a linear stepper motor as shown in Figure 1. The stepper motor consists of two orthogonally placed thermal actuator arrays connected to a yoke. The yoke and actuation rack have mating teeth structures to couple the motor with the shutter. By timing the two actuator arrays appropriately, the shutter can be moved in either direction as shown in Figure 1. Under quiescent conditions, friction between the shutter and the underlying substrate is used for locking the shutter in place [2].

Overview of the 3 poly surface micromachining technology

Surface micromachining refers to fabrication of mechanical structures on the surface of a silicon wafer using processes adapted from the IC fabrication techniques. Three dimensional structures are constructed by depositing multiple layers of poly (polysilicon) separated by glass (SiO_2) on the wafer. After processing is complete, glass is etched away leaving only the poly structures remaining as shown in Figure 4. The complexity of mechanical structures that can be constructed by this technique is dependent on the number of structural poly layers available. The prototype shutter/actuator was constructed using the commercially available 3 poly process called MUMPS provided by MCNC, North Carolina [1].

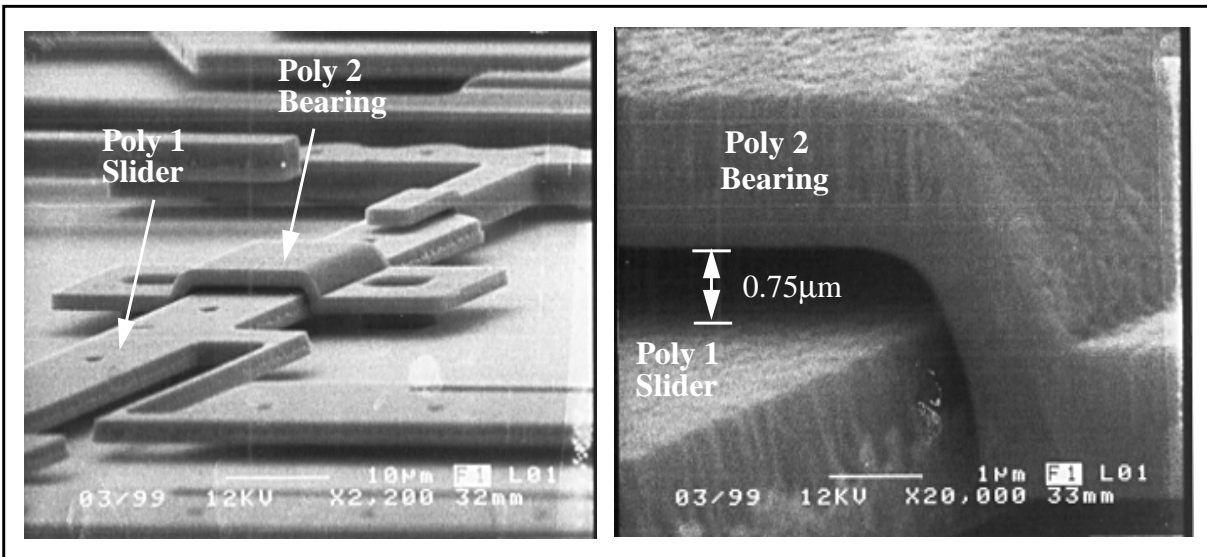


**Figure 4. (a) SEM micrograph of a surface micromachined poly 1 slider and a poly 2 bearing
(b) Enlarged view of the slider/bearing separation**

Shutter Design

The designed shutter is a 300μm by 1.2mm rectangular plate made of POLY1. The toothed rack is connected along the central axis. This allows a uniform distribution of force to the shutter for actuation. In order to permit the shutter to translate in only one axis, three flange type guide rails, were incorporated (see Figure 5) [3]. As shown, two guide rails are placed along the shutter edges while the third one is placed at the center of the rack. These three guide rails allow the shutter to move in one axis and at the same time prevent the shutter from pivoting about its center of gravity during translation. The flange of the guide rail is made of POLY2 with a 0.75μm separation from POLY1.

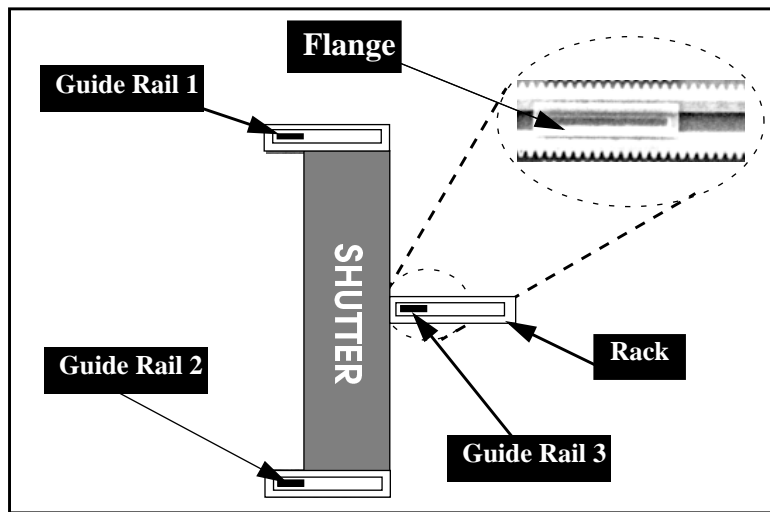


Figure 5. Shutter design

Linear Stepper Motor

The actuation mechanism is a linear stepper motor using thermal microactuators [4]. The actuators work on the principle of thermal expansion. The actuator is a U-shaped structure made of polysilicon with one arm wider than the other [5]. On passing a current through this structure, the narrower arm experiences a higher ohmic heating than the wider one. Consequently, the free end deflects as illustrated in Figure 6. Literature reports that such actuators are capable of generating around $5\mu\text{N}$ of force for 25mW of electrical power [6]. In order to attain greater driving force, these actuators can be coupled in a parallel arrangement [4].

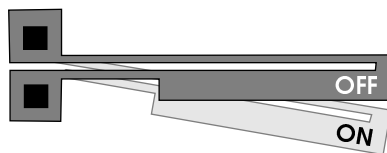


Figure 6. Operation of a U-shaped thermal microactuator

Figure 7 shows the layout view of the stepper mechanism. The mechanism consists of two sets of actuator arrays and a yoke. Array A consists of seven actuators and the array B comprises of 3 actuators connected in a parallel manner. The two arrays are arranged orthogonally and connected to the yoke via a flexure and a sliding joint. As a result of the orthogonal arrangement of the actuators, the yoke can be made to traverse in a clockwise or anti-clockwise path by appropriately timing the actuation signals.

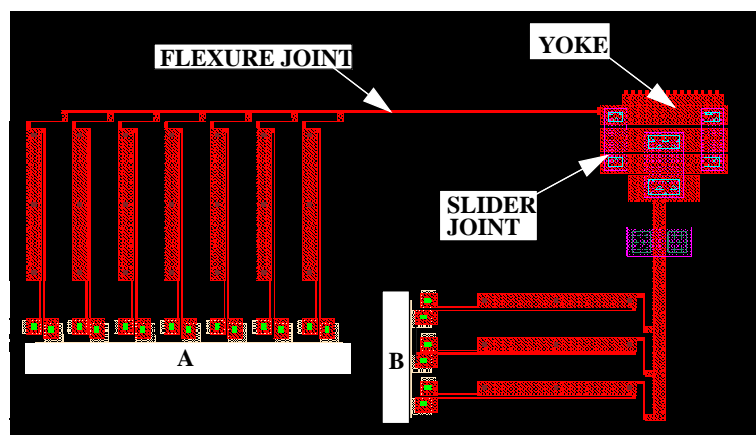


Figure 7. Linear stepper motor

The overall design is illustrated in Figure 8 and an SEM micrograph of the fabricated device is shown in Figure 9.

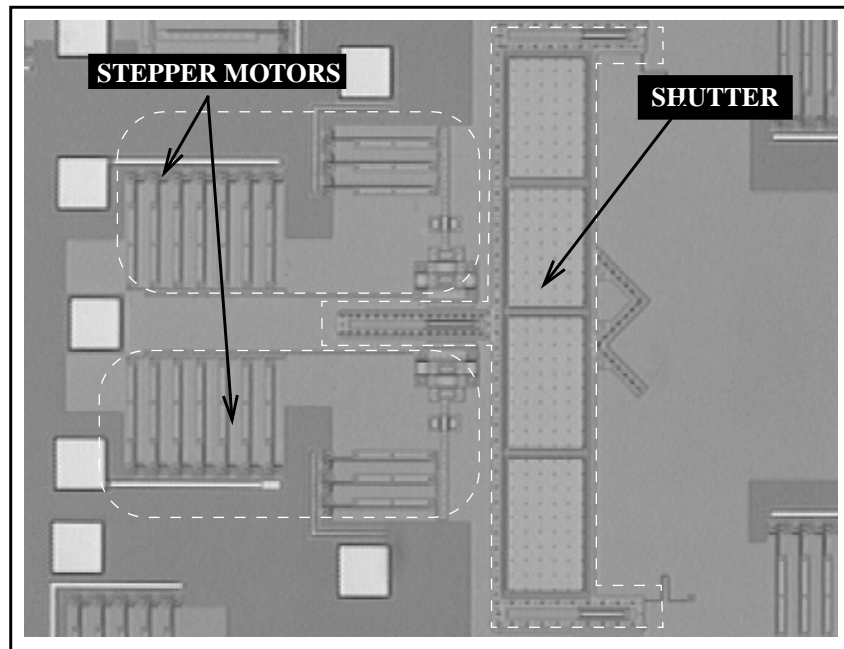


Figure 8. Micrograph showing the top view of the microshutter

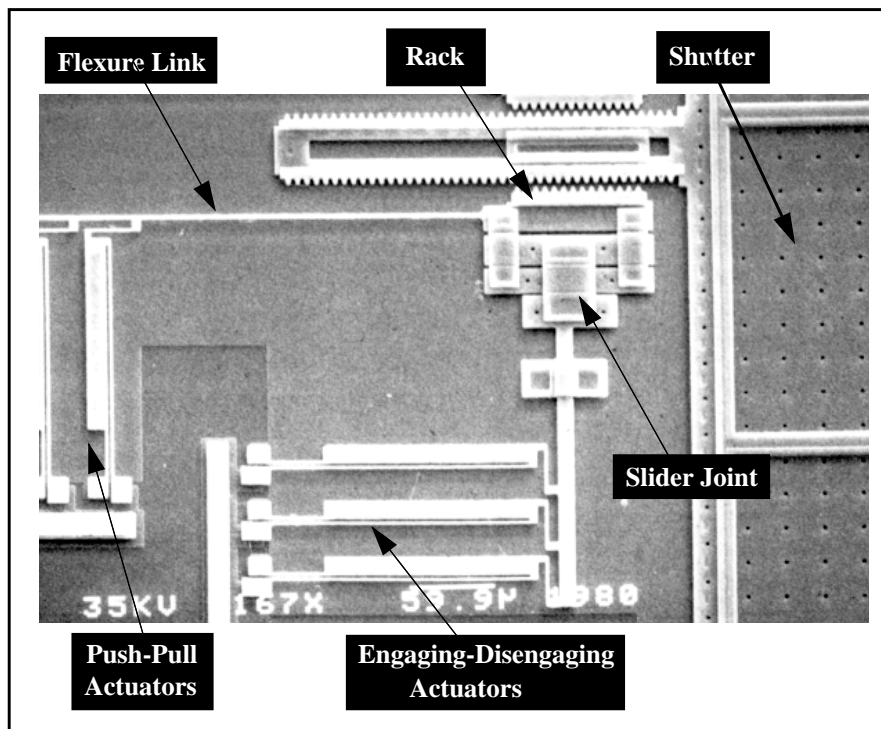


Figure 9. Scanning electron micrograph of the fabricated device

TESTING

In order to test the performance of the microfabricated shutter, an overlapping-phase test-signal was applied to the actuator arrays. The motion of the shutter was observed through an optical microscope. The two-phase signal was generated using a free running 555 timer circuit and a pair of T flip flop's as illustrated in Figure 10. In order to provide sufficient drive current, a single stage transistor switch was added to the output of the flip flop. The timer circuit was designed to operate at 1Hz so that the operation of the mechanism could be inspected visually.

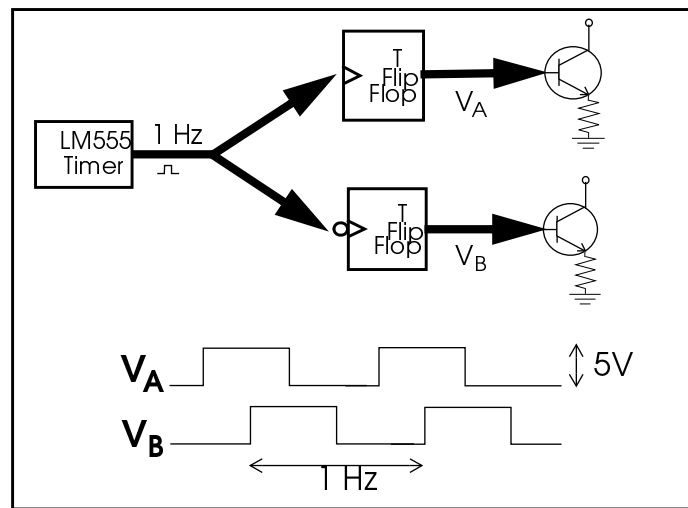


Figure 10. Schematic of timing circuit

The performance of thermal actuators is dependent on a number of design parameters [5,6]. Our actuators were seen to achieve their full stroke of $10\mu\text{m}$ while drawing 4mA at 6V. Actuator arrays however, being in a parallel connection, require a higher voltage signal to achieve the same stroke as individual actuators. To translate the shutter by $200\mu\text{m}$, 20 actuation cycles were required with each cycle consuming approximately 300mW of power. For our design, a 7 actuator array provided sufficient force to overcome friction and drive the $300\mu\text{m}$ by 1.2mm shutter. However, further work needs to be done to characterize the force requirements of different sized shut-

ters.

Problems Encountered

It was observed that reliable actuation can be provided to the shutter as long as the stroke of the actuators matched the pitch of the gear teeth (see Figure 11a). Any difference between the actuation stroke and gear pitch results in the tips of the rack and yoke teeth to line up with each other and prevent meshing of the teeth (see Figure 11b). Although this meshing problem can be avoided by electronically fine tuning the lateral stroke to match the teeth pitch, a rugged mechanical design would be preferred. New designs are being looked into to address this problem.

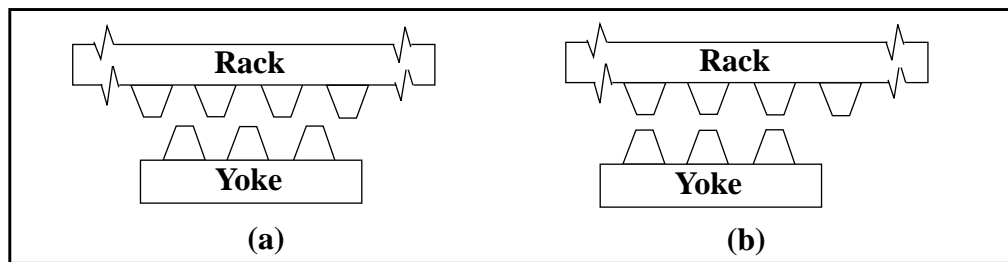


Figure 11. Teeth alignment during actuation for (a) proper meshing and (b) improper meshing

ONGOING WORK

A major concern with the present design is the low fill factor (ratio of slit area to the overall area) of 30%. Optimizing the present design will improve the fill factor but not by a dramatic amount. To take the fill factor closer to the 50% mark, we have redesigned the actuation mechanism. In the new design, vibrating thermal actuators are made to impact the sidewalls of the shutter. As shown in Figure 12, two pairs of thermal actuators are laid out at a 45° angle to the shutter sidewall. The upper pair causes the shutter to slide up (uncover the slit) while the lower pair causes the shutter to slide down (covering the slit). The actuation mechanism is much simpler and requires lesser real estate. A prototype device based on this design is currently being fabricated.

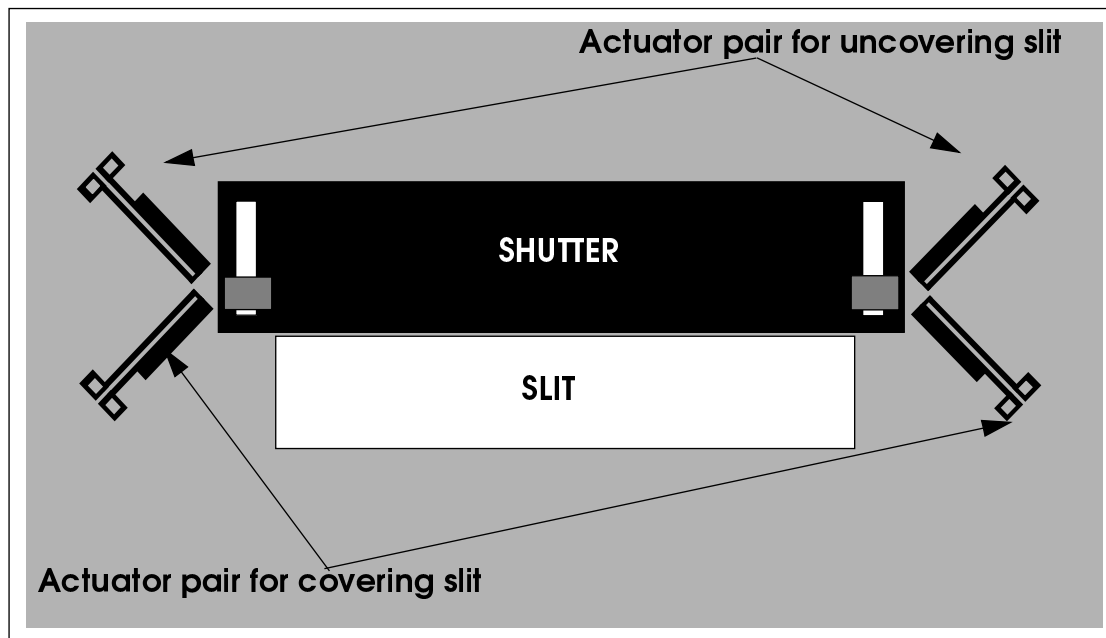


Figure 12. Vibromotor based actuation

CONCLUSION

We have demonstrated a prototype device using a thermal actuator based stepper motor combined with a slider mechanism to translate a shutter. A deep RIE silicon etch process can be combined with our design to create the opening and form the slits. This is being currently investigated. A new vibrating actuator based actuation mechanism has also being explored. The new actuation mechanism is much simpler and would result in a higher fill factor.

ACKNOWLEDGEMENTS

The authors gratefully acknowledge the services provided by the Canadian Microelectronics Corporation (CMC) for MUMPS technology. We also thank Dr. A. Carson for SEM analysis of the micromachined device and the staff of the National Research Council of Canada, Victoria for valuable suggestions. This work is jointly supported by funding from NRC and NSERC.

REFERENCES

- [1] D. Koester, R. Mahedevan, A. Shishkoff and K. Marcus, *Multi User MEMS Processes (MUMPS), Introduction and Design Rules rev. 4*, MCNC MEMS Technology Applications Center, Research Triangle Park, NC 27709, USA, July 1996
- [2] O. Solgaard, M. Daneman, N. Tien, A. Friedberger, R.S. Mueller and K.Y. Lau, "Opto-electronic packaging using silicon surface-micromachined alignment mirrors," *IEEE Photonics Technology Letters*, vol. 7 (1), January 1995, pp. 41-43
- [3] LS Fan, YC Tai and R.S. Muller, "Integrated Movable Micromechanical Structures for Sensors and Actuators," *IEEE Transactions on Electron Devices*, vol. 35 (6), June 1988, pp. 724 - 730
- [4] J. Comtois and V. Bright, "Surface Micromachined Polysilicon Thermal Actuator Arrays and Applications," *Solid State Sensor and Actuator Workshop*, Hilton Head, South Carolina, USA, 1996, pp. 174 -177
- [5] J. Comtois, V. Bright and M. Phipps, "Thermal Microactuators for Surface-Micromachining Processes," *Proc. SPIE: Micromachined devices and Components*, 23 - 24 October, 1995, vol. 2642, pp. 10 - 21
- [6] J.R. Reid, V.M. Bright and J. Comtois, "Force Measurements of Polysilicon Thermal Micro-Actuators," *Proc. SPIE*, 1996, vol. 2882, pp. 296 - 306

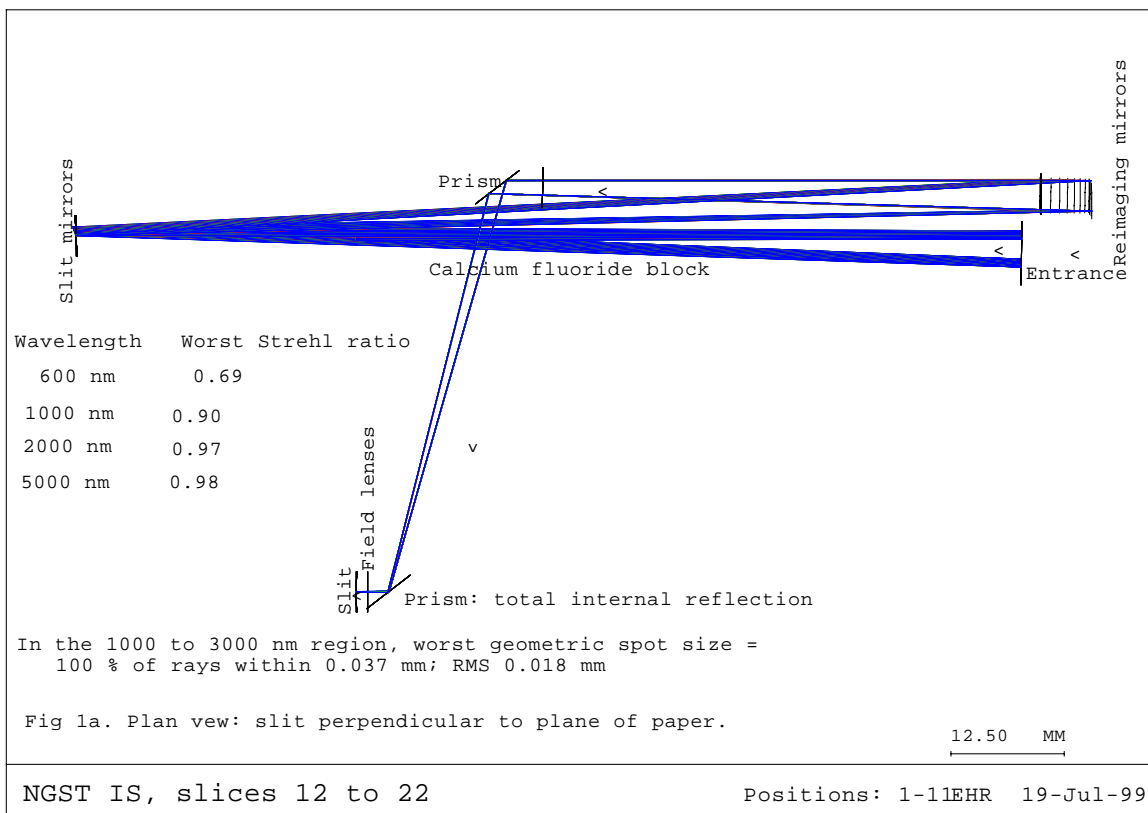
A SOLID BLOCK IMAGE SLICER FOR NGST`

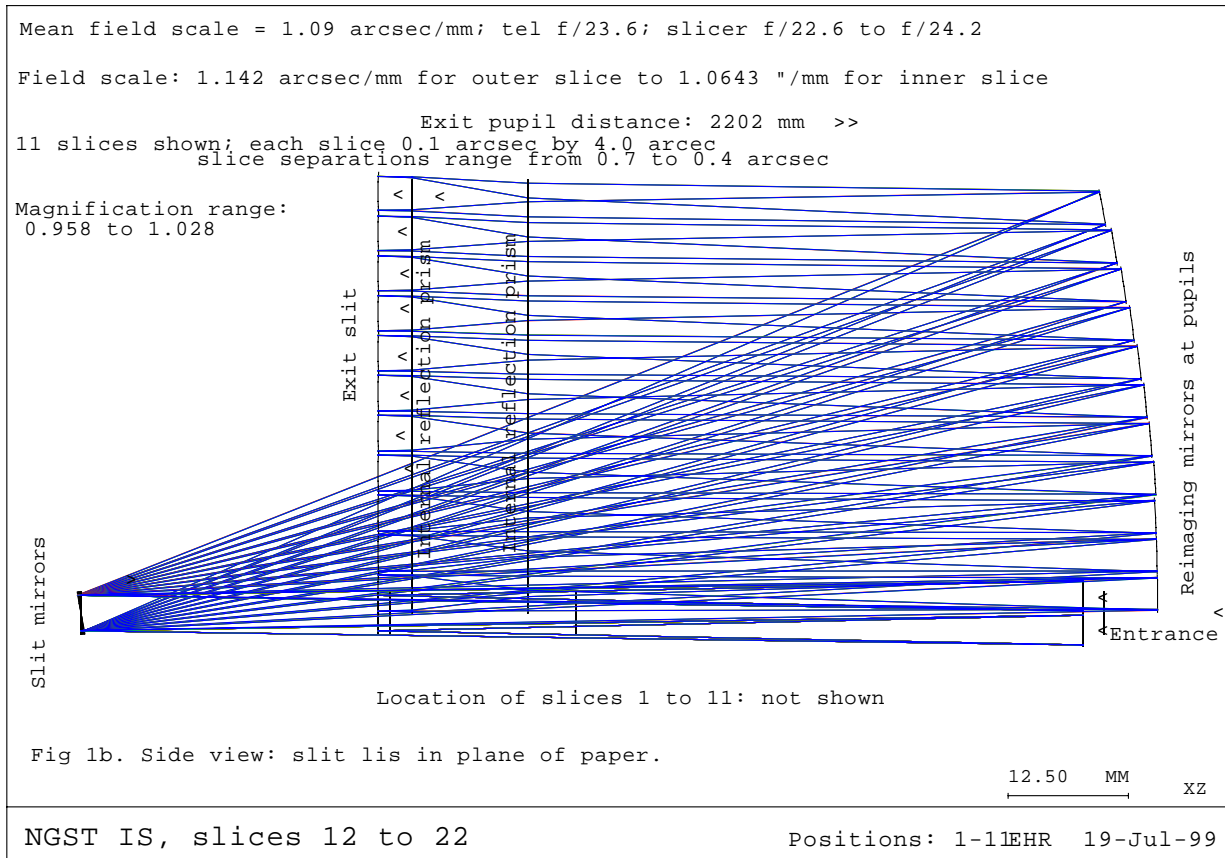
E.H.Richardson

1. Optical layout

Image slicers of the type that can sharply focus the sky onto the slit of a spectrograph require three powered optical elements in the light path for each slice. In the reflecting design outlined here, the first mirror is in the form of a reflecting slit located where the sky is focused by the telescope. This tilted, concave slit-mirror focuses the primary mirror (pupil) of the telescope onto a concave re-imaging mirror, which in turn focuses the sky (the slit mirror segment) onto a field lens where the slit of the spectrograph is located. Each slice of the sky requires a set of these micro-optics, as shown in Figure 1a where the slit is perpendicular to the paper and in Figure 1b which is a side view where the slit is in the plane of the paper. The slit mirrors are located side-by-side (Fig 1a) but the images of the slit mirrors are aligned end-to-end (Fig 1b) along the slit of the spectrograph by the tilted re-imaging mirrors. Thus the light from a two-dimensional object or field of stars is re-arranged so that it can enter the long, narrow slit of a spectrograph. Eleven of the 22 slices are shown in the figures. The optical prescription is available in both CodeV and Zemax formats.

The design shown in Figures 1 a, b uses back surface mirrors for the first two optical elements in a path, and a lens for the third. These optical surfaces could either be cemented or etched onto the outside of a single block of glass. The entrance surface of the slicer is above the focal surface of the telescope, and the slit mirrors are below the surface. Two prisms with total internal reflection are used to bend the beam so that the exit slit of the slicer is on the focal surface of the telescope. Thus no changes would be needed to either the telescope focus or to the collimator of the following spectrograph when the slicer is inserted. However, these prisms could be eliminated if the spectrograph were never used with the bare telescope, or if it were designed for slits at different axial distances from the bare telescope focus. (For example, if the slicer were to be used with a spectrograph which was also to be fed by slits illuminated by fibers with a minimum of bending of the fiber, the exit from the fibers might be below the telescope focal surface.) In that case, it can be seen in the drawings that if the two prisms were removed then the exit slit of the slicer would lie beside the rectangular set of entrance slit mirrors. This would have the advantages of reducing the width of the slicer and decreasing the cost (but it would not increase the transmission because the prisms are totally internally reflecting and thus have 100% reflectivity).





The slit mirrors and the field lenses have spherical surfaces but the re-imaging mirrors are toroidal, resulting in a spatial resolution within the slices which is diffraction limited at 1 micron. For an 8 meter telescope the FWHM (Full Width at Half Maximum) of the Airy disc is 0.06 arcsec at 2 microns. That is the wavelength where the telescope is specified to be diffraction limited, i.e., where the Strehl ratio of the images is better than 0.8 (the Strehl ratio is the ratio of the intensity of the core of the diffraction pattern (Airy disc) compared with that of a perfect optical system). The mirrors, which are metal coatings deposited on the outside of the glass, are illuminated by light inside the glass, thus the outside of the mirrors can be sealed from possible contact with contaminants. To summarize, the image slicer design has only two air/glass surfaces and only two internal reflections are required. It can be fabricated from a single solid block and hence is inherently very stable.

2) Location of Exit Pupil

Most telescopes are designed to be telecentric but the design given in the NGST “Yardstick” design is not. The location of the exit pupil of the image slicer can be adjusted by changing the tilts of the slit mirrors and the location and tilts of the re-imaging mirrors. In the design shown, the exit pupil is made

to be at the location of the exit pupil of the "Yardstick" NGST, which is 2.2 meters before the focal surface (but which will probably be changed). The slicer is versatile in the location of the exit pupil which thus can be matched to an optimum entrance pupil location for a given spectrograph design.

3) Field of View and Range of Field Scales

Each slit mirror is 4 arcseconds long and 0.1 arcsec wide. Thus the 22 mirrors have a total aperture of 4 by 2.2 arcsec on the sky which is transformed by the re-imaging mirrors to 88 arcsec by 0.1 arcsec at the slit of the spectrograph. To prevent information from the ends of individual slices from overlapping, a small (0.5 arcsec) gap was intentionally introduced between each slice when it is projected onto the output slit. Hence the total length of the slit in the notional design is 99 arcsec or 91 mm.

The field scale at the focus of the F/24 NGST telescope is 1.09 arcsec/mm which is also the mean scale at the output of the image slicer. However, the scales in individual slices in our design range from 1.14 for the outermost slices to 1.06 arcsec/mm for the two innermost slices. This is because of the differences in light path from the slit-mirror to the re-imaging mirror to the output slit for the various slices. This change of field scale would not significantly affect the scientific performance of the slicer and so was judged acceptable.

The variation of scale depends on the angle and so it increases if the total slit length were to be increased, i.e., if additional slices are added or if the length of each slice is increased. If required, the change in scale could be reduced by segmenting the internally reflecting folding prisms and repositioning the individual prisms to increase the distance from the outer re-imaging mirrors to the slit to equal the distance from the inner ones resulting in unit magnification for all slices. A design incorporating this refinement was done as an option for an image slicer with longer slit lengths for the GMOS spectrograph of the Gemini telescope. However, to reiterate, we believe this complication is not necessary for the NGST image slicer.

4) Sensitivity to Temperature Change

The solid block design has several advantages, especially for an image slicer that will be subjected to a large change of temperature.

Because the structure is made of the same material as the optical surfaces, thermal expansion or contraction would apply equally to the curvature of the surfaces and to their separations, thus the mirrors would stay exactly in focus. The lenses, however, would not remain exactly in focus because the index of refraction does not decrease as much as the lens curvature. In our design, however, the defocus of the exit pupil is minimal and could be eliminated altogether at operating temperature by specifying less curvature at room temperature when the lens is made so that it is optimal when the lens is cooled. The focal length of the lens is not critical because it serves simply as a field lens.

The variation of the index of refraction, N , of the glass with temperature will change the apparent location of the slit mirrors as seen from the telescope. However, the temperature-induced change of N

is ten times smaller than the change of N over the wide wavelength range of 1 to 5 microns. For a drop in temperature of 238 degrees, the wavelength-induced change in N is 0.03 compared with the temperature induced change, of 0.0025, given $dN/dT = -10.6\text{e-6/degC}$. The thermal contraction of the CaF in the 104 mm between the flat entrance surface and the slit-mirrors is 0.47 mm, the coefficient being 18.85e-6/deg . However, the decrease in N multiplied by that distance is 0.26 mm, thus the net defocus is only 0.2 mm. The resulting image blur is this number divided by the focal ratio in the CaF which is $F/34$ and so will be 6 microns, i.e., much smaller than the slit width of 100 microns. Although not necessary, mounting the slicer at the best focus for 35K could compensate for this small defocus effect. Alternatively, the telescope focus could be changed by 0.2 mm - it would probably need refocusing anyway because of the much larger focal change by contraction of the telescope structure.

In summary, the focus of the image slicer is insensitive to temperature changes.

5) Light Loss

There are only two air-to-glass (or vacuum-to-glass) surfaces in the light path, plus two metal reflections. If calcium fluoride, whose index of refraction at 2 microns, $N=1.424$, is used as the material, the loss by reflection at the refractive surfaces would be 3% per surface. This is less than for most glass types, and could be reduced even more with an anti-reflection coating of magnesium fluoride. Depending on wavelength, the resulting residual reflectivity would vary from 2.0% to 2.6%. Because the index of refraction of calcium fluoride is low, differing by only 0.05 from the magnesium fluoride coating, there is little reduction in reflection loss by an anti-reflection coating, but it would provide additional protection. The reflectivity of the silver or gold mirrors would be about 98% per surface, thus the total light loss at optical surfaces would be less than 10%.

6) Consequences of Choice of Glass Type

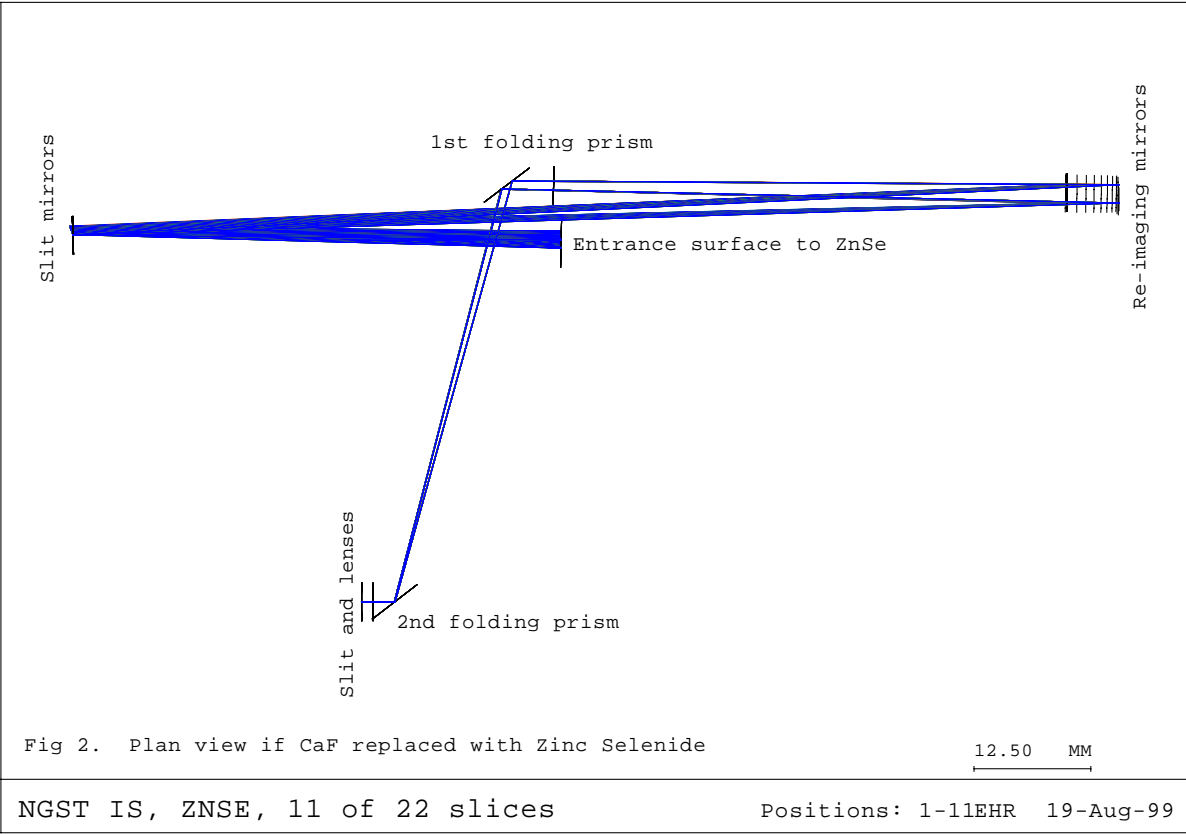
Other glasses were explored as alternatives to our initial choice of CaF. If a high index infrared transmitting glass such as Zinc Sulfide (whose $N=2.26$ at 2 microns) is used instead, the reflection loss at a bare air/glass surface is high: 15% per surface, or a 28% loss from the two surfaces. In this case, a MgF anti-reflection coating reduces the reflection by a large amount, to 1% at one selected wavelength where the reflections from the MgF and ZnS subtract. This is smaller than for coated CaF. However, a disadvantage of ZnS is that the reflectivity rises at other wavelengths, reaching 8.6% per surface, or 16% for the two surfaces. Thus, for a high index material an anti-reflection coating is essential, but the average reflection loss would still be higher than if CaF is used. Another good IR transmitting material is Zinc Selenide, but its N is even higher: 2.446 at 2 microns. The bare reflection loss per surface is 18%, thus 32% for the two surfaces. With a MgF anti-reflection coated at 2 microns the loss is reduced to 1.9% per surface, thus 3.8% for the two surfaces, but it rises to 10.5% at other wavelengths in the region, thus to 19.8% for the two surfaces.

The slicer in Figures 1a,b is designed for CaF but, if changed to another glass type with a higher index of refraction, it is necessary to change only the distance from the entrance surface to the slit mirrors. An example is shown in Figure 2. The re-imaging mirrors can be smaller with the high N glass because the internal focal ratio is longer: $24 \times 2.26 = F/54$, cf. $F/34$ with CaF. This simple re-design was also

done for other IR transmitting materials: silicon, barium fluoride and zinc sulfide. All deliver diffraction limited image quality.

A potential advantage of the higher index glasses, such as ZnSe, is that the angle of incidence onto the internally reflecting prisms can be increased without losing total internal reflection. Thus the first prism can be moved much further from the re-imaging mirrors. Consequently, the lateral distance to the exit slit can be decreased in proportion, and hence the image slicer can be narrower than for the CaF version, and block less of the focal surface, thus, for example, allowing fiber pickups to be positioned closer to the image slicer. Overall, however, CaF appears to be the best material for the NGST image slicer.

23:06:29



MODERATE RESOLUTION 1 to 5 micron SPECTROGRAPH FOR NGST

E.H. Richardson

1) Required Spectral and Spatial Resolutions

A design goal for the NGST Multi-Object Spectrographs is to have spectral resolutions, R , from 100 to 5000. However, analyses of the Design Reference Mission appear to indicate that resolutions in the 1000 – 3000 range are central and so it was decided to try to achieve this at 2 microns wavelength, with a slit width of 0.1 arcsec (projected onto the sky). The desired spatial resolution along the slit of the imaging spectrograph, at least for the image slicer application, is diffraction limited at 2 microns wavelength, to match the anticipated performance of the telescope. The pixel size of the InSb detector was assumed to be 27 microns since Bely, in the SPIE paper "The NGST "YARDSTICK MISSION", states "the final aperture ratio is $f/24$ to match the angular resolution of the telescope at 2 microns with a typical pixel size of about 27 microns").

At $f/24$, the field scale of an 8 meter telescope is 1.09 arc seconds per mm. The NGST will have a segmented primary mirror but, if the equivalent of a single mirror, the full width at half maximum of the Airy disc at 2 microns is 0.063 arcsec, thus 58 microns or approximately two pixels on the detector at $f/24$.

However, the image slicer was designed for a slit width of 0.1 arcsec and thus requires a $f/15$ spectrograph camera to match the spectral resolution of the detector in the direction of dispersion. In this case, the spatial resolution along the slit would be slightly under-sampled by the detector at 2 microns, but would be adequately sampled at wavelengths longer than 3.2 microns (because the diameter of a diffraction-limited image is proportional to the wavelength). The fixed width of the slit is a compromise, being larger than the Airy disc at 2 microns, but smaller than the Airy disc at wavelengths longer than 3.2 microns.

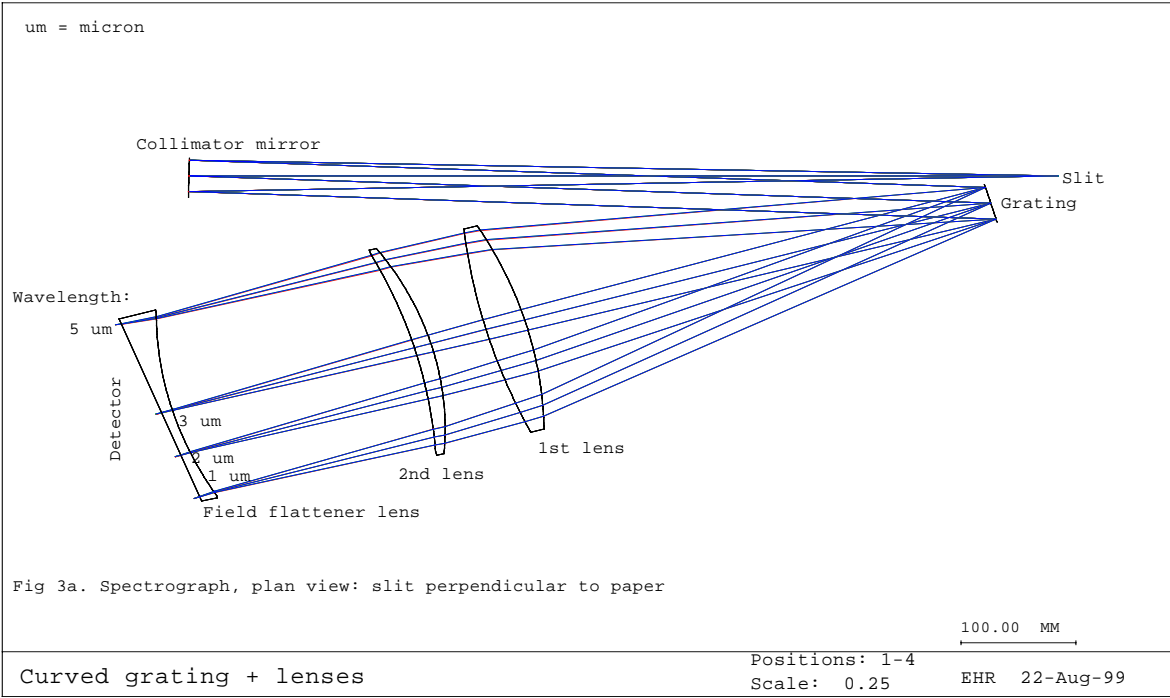
If a detector with 18 micron pixels were used with the spectrograph, the ideal focal ratio for a 2-pixel resolution match would be $f/18$, i.e., close to the nominal $f/15$ ratio of the spectrograph camera. In that case, at 2 microns wavelength, the spatial image would be only slightly under-sampled and the spectral resolution slightly over-sampled, the slit projecting to 3 pixels.

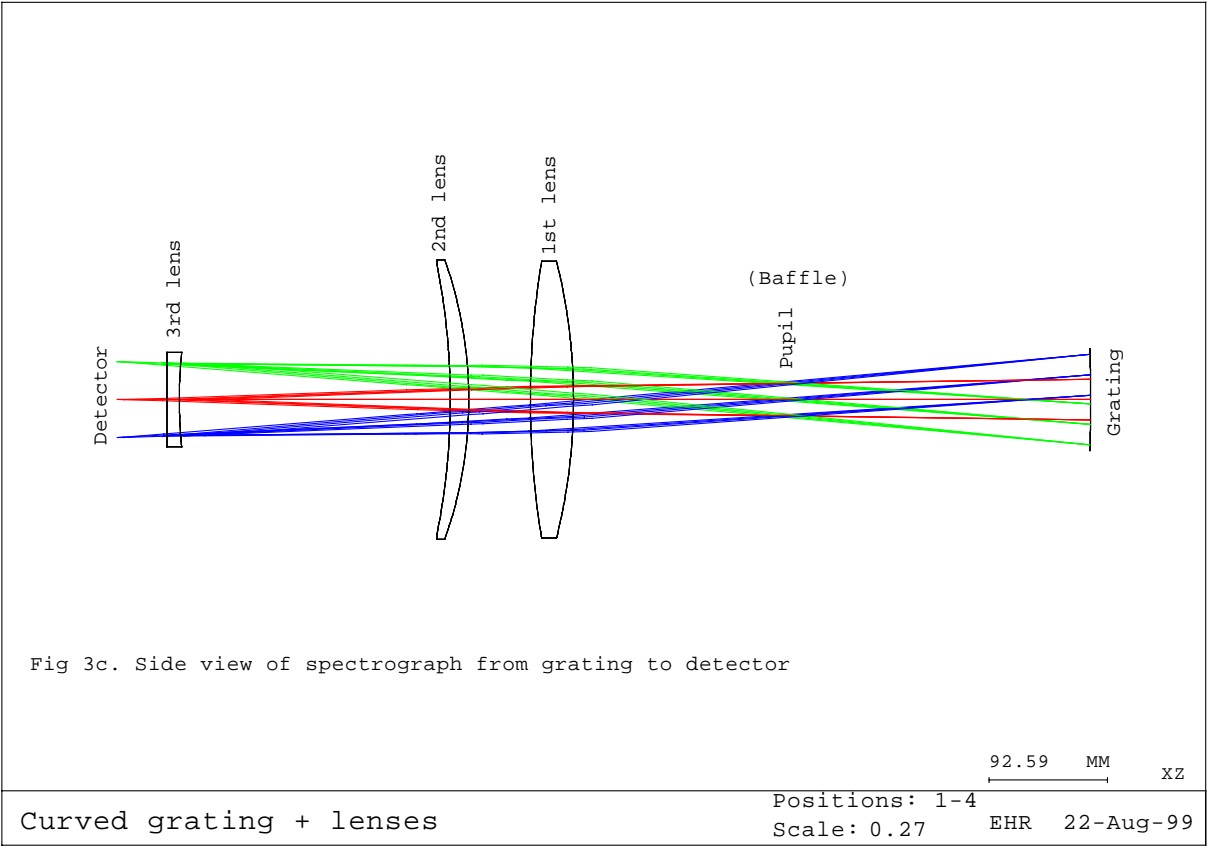
2) Optical Layout of a Simple Spectrograph Option for a Single Long Slit

Some options for spectrographs for NGST use Three Mirror Anastigmats (TMA) designs. These offer considerable versatility but require six or seven reflections within the spectrograph. Some designs (cf. ESO MOS/IFS study) also have additional mirrors in the fore-optics resulting in 13 reflections after the focus of the telescope, not including the grating, plus a refractive filter and possibly a window on the detector. These spectrographs in their "high resolution" mode are designed to cover only a portion of the required 1 to 5 micron wavelength region at a time. However, if it is acceptable to have a dedicated spectrograph that does not require changes in dispersion for different spectral regions, the number of reflections can be drastically reduced and the wavelength coverage increased.

One example is shown in Figures 1a, 1b and 1c. Fig 1a is a top view where the entrance slit and the spectral lines are perpendicular to the plane of the paper, and Fig 1b is a side view where the slit and the spectral lines are in the plane of the paper. These two drawings start at the slit, the optics preceding the slit are an 8-meter telescope with an f/24 output and an exit pupil located 2 meters before the focus of the telescope, which could include the solid block image slicer described by Richardson (1999)

20:49:31





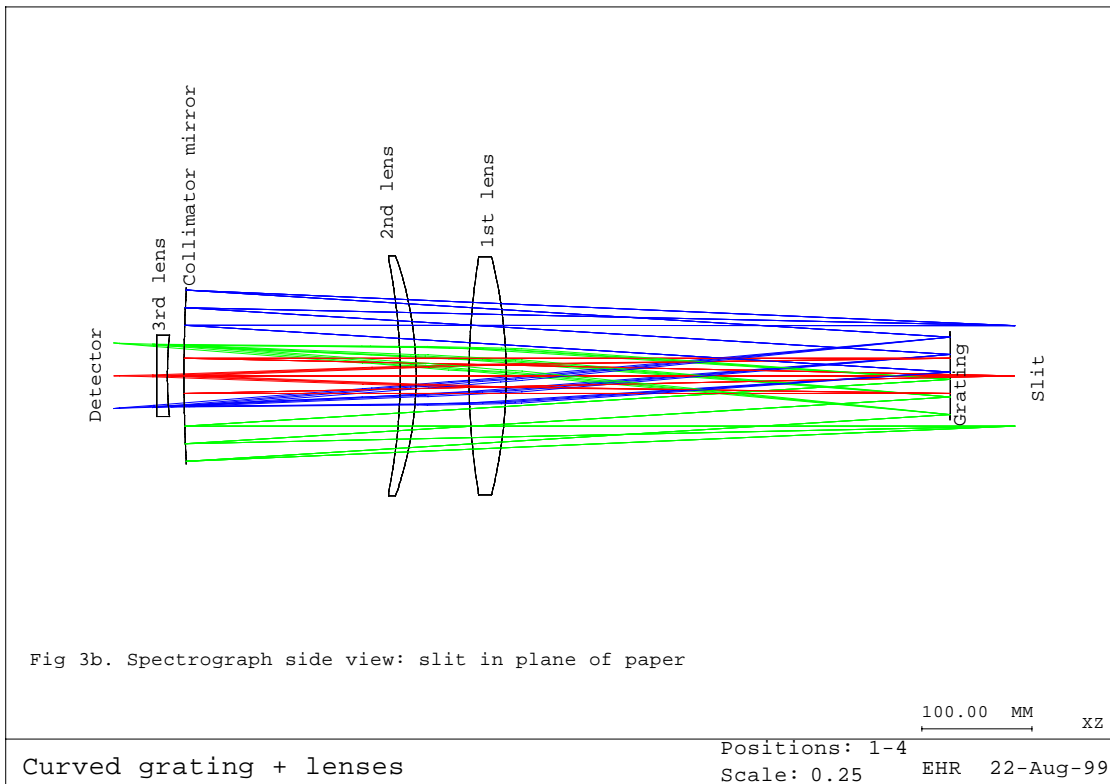


Figure 1: Three views of the proposed spectrograph

The collimator of this spectrograph is $f/24$, which is the same as that of the output of the NGST and the output of the image slicer. This long focal ratio simplifies the collimator design so that it consists of only one mirror (as is common in many astronomical spectrographs). The grating is concave and thus serves both as a dispersing element and as a focusing element in the camera of the spectrograph. The grating has 100 grooves/mm. It could be interchanged with gratings with different blazed wavelengths to enhance priority wavelength bands. The grating is followed by three lenses, which can also serve as filters. The field flattener lens close to the detector could also serve as a protective window and perhaps as an order sorter if given a suitable coating. The feasibility of wedged coatings for such use requires investigation.

The images are diffraction limited from 1 to 5 microns wavelength. The dispersion is 21 NM/mm and so for 27 micron pixels, $R = 3000$ at 3.6 microns. The length of the spectrum is 190 mm and the length of the spectral lines is 60 mm in this notional design. The angular length of the slit is 100 arcsec (similar to the image slicer) but could be longer. A design with a 164 arcsec (151 mm) long slit has been evaluated and is satisfactory.

Because the telescope outlined in the Yardstick Design is not telecentric (i.e., does not have a very distant exit pupil) and because the spectrograph collimator consists of only one mirror, the exit pupil is not imaged onto the diffraction grating, which is unusual. It can be seen in Figure 1c, which is a side view limited to the path from the grating to the detector, that the re-imaged pupil is located about one

third of the distance from the grating to the detector. That would be a convenient place to place a baffle.

The distance from the slit to the collimator is 0.75 meters, which is well within the space available for instruments. The optical prescription for this spectrograph is available in both CodeV and Zemax formats.

This spectrograph design which incorporates a refractive camera will not work well for a wide range of spectral resolutions unless the last lens element is changed when the grating is changed. Panchromatic reflecting camera designs are now being investigated to provide more versatility.

3) Minimum Required Width of Grating

Some spectrograph design options, such as those in the ESA MOS design, have large gratings, 140 mm wide, which is much bigger than necessary for the required spectral resolution (in the case of the ESA HR (high resolution) spectrograph, the collimated beam was made large to suit the optical design, not because it was required to achieve the resolution.)

For a grating, the spectral resolving power, $R = \lambda / (\Delta \lambda) = W / s$, where W is the width of the grating and s is the separation of adjacent grooves. In our case, if both λ and s equal 2 microns, and if $R = 3000$, then $W = 6$ mm, a very small grating. Although gratings with $s = \lambda$ are available, it is more usual to have $s \sim 2 \times \lambda$. Also, if the same grating is to be used at longer wavelengths, say to 5 microns, the choice of width of the grating should be $s = 10$ microns. This implies that W should be about 30 mm. Note that the width of the grating in our design, 34 mm, is larger than the theoretical minimum but is still small compared with the 140 mm wide grating in some of the other NGST spectrograph designs.

To achieve $R = 3000$ at 2 microns requires that each pixel cover 0.33 micron (for 2 pixels per resolution element), thus the dispersion would be $0.33 / 0.027 = 12.3 \text{ nm/mm}$ for 27 μ pixels.

In the spectrograph design described above, the dispersion was selected to be 21 nm/mm, thus it is at the wavelength of 3.4 microns that the spectral resolving power of 3000 is achieved. The width of the grating is 34 mm, the groove spacing is 10 microns (i.e., 100 grooves/mm), and the angle of incidence is 18 degrees. This increases the width of the beam in the direction of dispersion by $1 / (\cos 18)$. The angle of diffraction is negligible at 1 degree. The effective focal ratio of the camera is $f/14$ in the direction of dispersion and $f/15$ perpendicular to dispersion. In this imaging spectrograph, the spatial field scale of the 8 meter telescope at the focus of the spectrograph is 1.75 arcsec/mm and so the spatial resolution (2 pixels) is 0.09 arcsec at 2 microns wavelength.

4) Multi-Slit Spectrograph Designs

One approach to having several slits feeding the same spectrograph is to use a three-mirror collimator (TMA). However, the separation of slits such as those at the outputs of fiber feeds can be positioned and tilted to send the beam in different directions and so a collimator mirror could be associated with each of the fiber feeds. Thus, instead of having a large TMA, an array of single collimator mirrors is

possible, thus eliminating two reflections in the light path. Design work on such a spectrograph is still proceeding.

References

Richardson, E.H. et al. 1999 in "3D Spectroscopy", ASP Conf. Series, in press, and in Appendix B7 of the Canadian NGST MOS/IFS report.